Mapping Dark Matter Distributions in High Extinction Galaxy Clusters

Case Study of RXCJ0524.4+0819

Aaron Jennis

Under the guidance of Ian Dell'Antonio

A thesis submitted in partial fulfillment of the requirements for the degree of Bachelor of Science

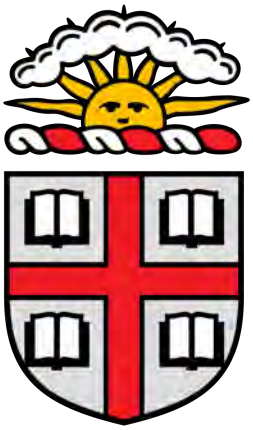

Department of Physics
Brown University
Providence, RI, USA
April 2021

Mapping Dark Matter Distributions in High Extinction Galaxy Clusters: Case Study of RXCJ0524.4+0819

Aaron Jennis *

May 2021

Abstract

Gravitational lensing is a powerful tool for investigating massive structures in the Universe. Through the development of deep wide-field surveys, it has become possible to leverage the statistical nature of weak gravitational lensing to reconstruct the total matter distributions of galaxy clusters. For the most part, researchers have steered away from studying clusters near the galactic plane due to higher concentrations of dust and bright stars along the line of sight. These factors make high extinction galaxy clusters more difficult to image and accurately analyze. In this study, we present the first measured weak lensing signal of the high extinction cluster, RXCJ0524.4+0819. We use these findings to map the dark matter distribution, plot the shear profile, and estimate the mass of the cluster. Our values are consistent with the previous empirical X-ray estimate of this cluster's mass, opening up the possibility of expanding weak lensing surveys to more high extinction clusters.

Keywords: dark matter; weak gravitational lensing; galaxy clusters; high extinction;

*In collaboration with and advised by Professor Ian Dell'Antonio, Astrophysics and Observational Cosmology Group, Department of Physics, Brown University, Providence, RI, USA

Contents

Acknowledgements

First and foremost, I would like to thank Professor Dell'Antonio for his continued guidance, support, and patience throughout both this past year and my previous summers in his lab. I am also grateful for his first introducing me to the world of physics research five years ago. I could not have made it to this point without his consistent help and advice. Thank you to Professor Pelcovitz for first connecting me with Professor Dell'Antonio.

I would like to thank Shenming Fu for his work on the image processing pipeline which was indispensable to my research and for his diligent help debugging errors. I also want to thank Professor Valles for his thoughtful advising these last two years and for providing me and many others with an exciting and accessible entry into the world of physics.

Lastly, thank you to my family and friends for all their support these last four years at Brown.

List of Figures

1 Introduction

The search for dark matter is one of the most active areas of astrophysics and cosmology research. Dark matter constitutes approximately 27% of the mass-energy density of the Universe—over five times that of baryonic matter's contribution—yet much about its true nature remains unknown. This matter is "invisible" as it does not interact with light, only gravitationally. Physicists are consequently left to detect dark matter indirectly through the gravitational effect it has on its environment. This can be done through the phenomena of gravitational lensing, the bending of light by a massive gravitational body. This distorts the light source's image, either as *strong* or *weak* lensing, depending on the geometry and lens' mass.

Galaxy clusters are ideal laboratories for using this effect to study dark matter. First, with masses on the order of 10^{14}–$10^{15} M_{\odot}$, galaxy clusters are the largest gravitationally bound structures in the Universe [1].[1] Thus, they are capable of producing detectable lensing signals, both strong and weak. The first observation of a galaxy cluster as a gravitational lens came in 1986, when two independent research groups measured strongly lensed luminous arcs that were located at a much higher redshift than the cluster itself [2]. Second, galaxy clusters are comprised of predominantly dark matter. In fact, only $\sim 3\%$ of the cluster's mass is in the form of stars (within hundreds to thousands of individual galaxies) and $\sim 15\%$ is located in the gas between the galaxies (the intracluster medium). The remaining $\gtrsim 80\%$ is dark matter, situated in large roughly spherical structures called *dark matter halos* [2–4]. Under the current ΛCDM cosmological model, these halos formed through hierarchical clustering [1]: Small quantum fluctuations in the early Universe expanded exponentially during inflation, resulting in non-negligible overdensities throughout space. Over time, these overdensities collected dark matter, which gravitationally attracted more dark matter and eventually baryonic matter. Initially small accumulations of dark matter merged to form larger ones through a "bottom-up" process, leading to the cluster-sized halos and subhalos we observe today.[2] Thus, galaxy clusters and models of dark matter are inherently intertwined.[3]

Still, our model of how galaxies and clusters form and evolve is not complete. To solidify our understanding will take combined efforts in theory, simulations, and observations of clusters at a range of redshifts. These studies also have significant implications for cosmology, as galaxy clusters correspond to "peaks in the large-scale matter density" [3, p. 2] and thus map the large scale structure (LSS) of the Universe [6]. As reflected in their substructure, galaxy clusters have dynamical time scales "not much smaller than the Hubble time - so that they retain a 'memory' of their formation - render[ing] them of particular interest for cosmologists" [4, p. 31]. Furthermore, the number density of galaxy clusters, particularly as a function of mass and redshift, provide constraints on cosmological parameters and dark energy [1, 2, 7]: "accurate measurements of cluster masses provide a cornerstone of cosmological work" [3, p. 22].

[1] *Superclusters* of galaxies of are not gravitationally bound.

[2] We observe more substructure at higher redshifts, because those clusters have had less time to smooth out and mergers were more common earlier in the Universe [1].

[3] For an in-depth review of galaxy cluster formation, see [5].

There are a number of distinct methods commonly used to estimate the mass of galaxy clusters, such as X-ray measurements of a cluster's gas (Section 2.2) and the thermal Sunyaev-Zeldovich effect. However, these techniques make assumptions about the hydrostatic equilibrium and spherical symmetry of the clusters which are not always valid. In an attempt to avoid the reliance on dynamical assumptions, strategies have been devised to use measurements of the intensity of the lensing signal to derive the cluster's projected mass distribution. In the case of weak lensing, this is particularly challenging as the distortion of any single source is small compared to its intrinsic shape. This is compounded by the fact that the atmosphere and observational instrument itself introduce additional effects that obscure and mask the signal we are trying to measure. In turn, these studies make use of the statistical nature of weak lensing and measure the average tangential ellipticity alignment of background sources to learn about the cluster doing the lensing. If calibrated properly, weak lensing offers an unique, unbiased method for mapping the surface mass density of galaxy clusters, independent of any astrophysical assumptions about the dynamical state, baryonic behavior, or star formation rate of the cluster—a more direct probe of the total matter distribution of clusters [6]. It is valuable to compare the results from weak lensing measurements to the measurements from other methods, such as X-rays—the goal being to quantify the bias in traditional X-ray estimates and calibrate a scaling relation between the weak lensing mass and directly observable quantities [1, 8].[4] Over the last three decades, gravitational lensing has become a powerful technique for studying galaxy clusters, providing a window into the unseen world of dark matter.

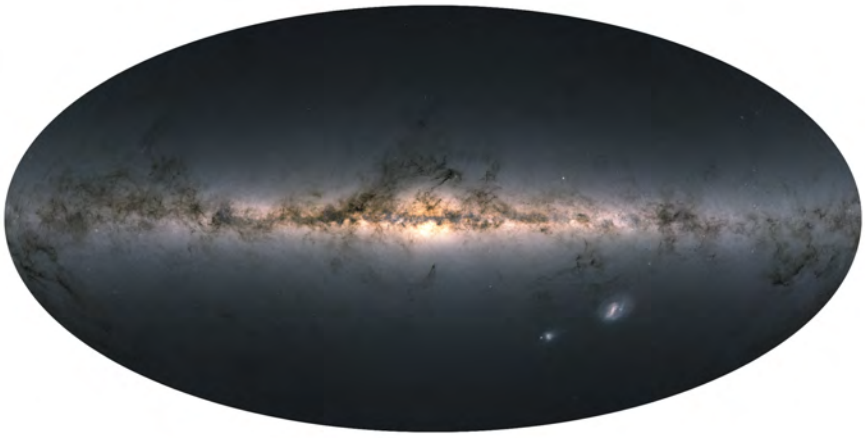

Figure 1. Map of the Milky Way from Gaia Data Release 2. Note the increased star density along the galactic plane. *Source:* ESA/Gaia/DPAC

In this study, we look at the weak gravitational lensing signal of the high extinction galaxy cluster RXCJ0524.4+0819, which has not before been measured. High extinction clusters have

[4]Clusters regularly have a brightest cluster galaxy (BCG) in their centers, often a type-cD galaxy [2]. This large elliptical galaxy is a useful point of comparison between the lensing, X-ray, and optical peaks; offsets can provide insight into the cluster's dynamical state and constrain models of self-interacting dark matter (SIDM) [1, 7, 9].

largely been avoided by lensing studies because the significant amount of dust along the line of sight makes it more difficult to obtain accurate measurements (Section 2.1).[5] This relatively higher concentration of dust (and bright stars) is a result of the cluster's line of sight lying close to our galactic plane (see Gaia's map of the Milky Way shown in Figure 1). Our goal is to see if we can successfully measure an accurate weak lensing signal from RXCJ0524.4+0819 and if so, use it to reconstruct the total matter distribution and estimate its mass. This study serves as an experiment in assessing the feasibility of studying high extinction galaxy clusters through weak lensing. If we strive to better understand dark matter and create a complete picture of the Universe's galaxy cluster distribution, we must meet the challenge of high extinction clusters head on.

In the next section, we review the background theory relevant to this research. In Sections 3 and 4, the data and procedural methods of the study are outlined in detail. In Section 5, the study's results are presented and analyzed. Finally, in Section 6, we summarize our findings, discuss their significance, and explore the opportunities for future related work.

2 Theory

2.1 Extinction

Extinction is the absorption and scattering of light by dust along the line of sight. This causes sources to appear dimmer by a factor of $e^{\tau_\nu(s)}$, where s is the distance from the source to the observer and $\tau_\nu(s)$ is the frequency-dependent optical depth in the direction of the source [2, p. 50]. This effect is thus dependent on wavelength, scattering blue light more readily, resulting in a reddening of the source as well [2]. Overall, images with more severe extinction are thus more difficult to derive accurate measurements from. The wavelength-dependent dimming of astronomical sources can be visualized in Figure 2.

The change in apparent magnitude is described by the *extinction coefficient* (units of magnitudes) as follows:

$$A_\nu \equiv m - m_0 = 1.086\tau_\nu \ , \tag{1}$$

where m is the apparent magnitude with extinction and m_0 is the apparent magnitude without extinction [2]. Similarly, the change in color index is described by the *color excess* as follows:

$$E(X-Y) \equiv A_X - A_Y = (X-Y) - (X-Y)_0 \ , \tag{2}$$

where X and Y are two filters, $(X-Y)$ is the observed color with extinction, and $(X-Y)_0$ is the intrinsic color without extinction [2, 11]. It is useful to define a *reddening parameter*, $R_X \equiv$

[5] One previous study that looked at a cluster with "severe extinction and stellar obscuration" is [10].

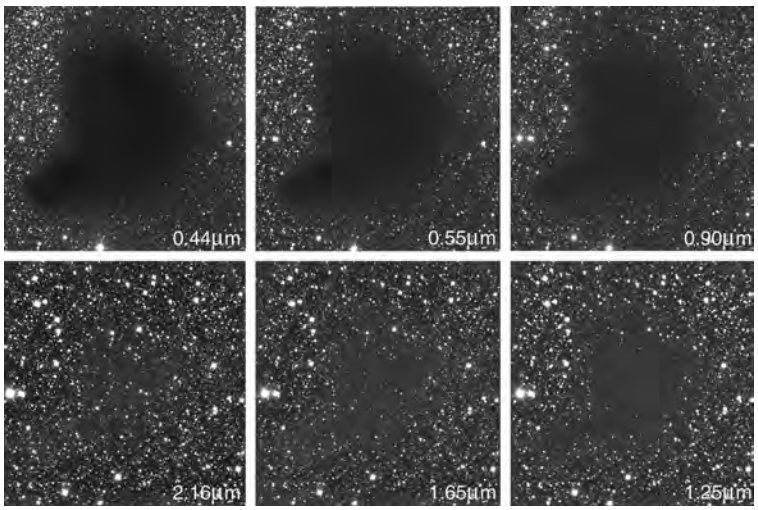

Figure 2. Extinction of background stars from the molecular dust cloud Barnard 68 (B68), containing mostly molecular hydrogen (H2). Images taken with increasingly red filters, clockwise from top left. *Source:* ESO

$(1 - \frac{A_Y}{A_X})^{-1}$, such that $R_X = \frac{A_X}{E(Y-X)}$ [2, 11]. It is also common to use blue (B) and visual (V) filters, which give [2]:

$$A_V = R_V E(B - V) \ . \tag{3}$$

These values are all dependent on the properties of the dust itself, such as grain size, composition, and density. For the Milky Way's interstellar dust, Equation (3) becomes: $A_V = (3.1 \pm 0.1)E(B - V)$ [2], although this value will vary depending on one's line of sight. In general, studying sources of known intrinsic magnitude and color, it is possible to estimate the *extinction curve* of a dust-filled region.

2.2 X-ray Mass Estimates

Galaxy clusters emit X-ray radiation from hot diffuse gas in the intracluster medium (ICM) [8, 12]. As mentioned in Section 1, this gas constitutes $\sim 15\%$ of the total mass of the cluster [4]. This radiation is predominantly in the form of bremsstrahlung. Bremsstrahlung (*free-free*) is emitted when one charged particle is decelerated as it passes by another charged particle. Clusters also emit some X-rays via recombination (*free-bound*) and line (*bound-bound*) emission from ionized metals. The ICM gas is relatively easy to observe because of how hot and bright it is. For clusters with masses $3 \times 10^{13} M_\odot < M < 10 \times 10^{15} M_\odot$, the gas is heated (from gravitational infall) to temperatures $10^7 K < T < 10^8 K$ (1–10 keV). Moreover, the X-ray luminosity, L_X, is generally between 10^{43}–10^{45} erg/s. Only active galactic nuclei (AGN) are brighter extragalactic X-ray sources, but clusters are very spatially extended, making them easily identifiable. [2, 3]

If the gas' temperature and density profiles are known, then the following expression can be

used to directly find the mass of a cluster within a radius r:

$$M(r) = -\frac{rk_BT(r)}{G\mu m_p}\left[\frac{d\ln n}{d\ln r} + \frac{d\ln T}{d\ln r}\right] , \tag{4}$$

where k_B is Boltzmann's constant, $T(r)$ is the gas' temperature, G is the gravitational constant, μm_p is the mean molecular weight, and $n(r)$ is the gas particle density [3].[6] (This formula also makes assumptions about the dynamics of the cluster, which we will discuss later in this section.) Unfortunately, in practice it is rather difficult to accurately measure the temperature and density profiles of the gas, as its spatial distribution is not completely homogeneous. On the other hand, alternative approaches such as the isothermal gas assumption ($T(r) = T_g$), β-model [14], and mass-velocity dispersion relation, yield comparatively poor results [2].

Instead, a suitable scaling relation between the X-ray luminosity and mass has been devised. Using the proportionalities of bremsstrahlung and approximating the gas density as $\rho_g \sim M_g r_{vir}^{-3}$, one can write the following relation: $L_X \propto f_g^2 M_{vir}^{\frac{4}{3}}$, where $f_g \equiv \frac{M_g}{M_{vir}}$ is the gas fraction. The early X-ray telescope ROSAT could only measure photons with energies less than 2.4 keV, so this relation became: $L_{<2.4\,keV} \propto f_g^2 M_{vir}$. Empirically testing this proportionality on many galaxy clusters, the following straightforward scaling relation was found:

$$L_{<2.4keV} \propto M^{1.5} , \tag{5}$$

where M is the total cluster mass [2, p. 314].[7] This fit is not quite as tight as the M–T relation ($M_{500} \propto T^{1.58}$), but again, the temperature is more difficult to measure than the luminosity [2]. For the X-ray mass estimates used in our sample, we use the MCXC catalog's [15] values, which are derived using a similar scaling relation as Equation (5) in going from L_{X500} to M_{X500}.

The prior methods for estimating the cluster mass based on its X-ray radiation make assumptions about the dynamical state of the cluster that are not necessarily always valid [16]. Mainly, both the scaling relations and Equation (4) assume that the cluster is in hydrostatic equilibrium (HSE). The most substantial disrupter of HSE is cluster-cluster merger events, which are not uncommon. These dynamic interactions drive the clusters out of equilibrium and cause additional gas heating which results in more emission. As Dahle states, "this [HSE] assumption is not always valid, as some clusters have complex temperature structures due to ongoing merging events" [12, p. 954]. Moreover, as mentioned in Section 1, galaxy cluster have long relaxation times [16], and will only return to equilibrium once one sound-crossing time[8] has passed since the most recent major merger event [2, p. 297]. These long relaxation times also help explain the substructure observed in many galaxy clusters; "$\sim$ 50% of clusters show some substructure in the X-rays" [6, p. 19]. These clusters have not fully smoothed out and relaxed into HSE, violating the other major

[6] There exist slightly different forms of this equation in the literature (e.g., [2, 13]).

[7] For the full derivation, see [2, pp. 313–314].

[8] "The sound-crossing time defines the time-scale on which deviation from the pressure equilibrium are evened out," [2, p. 297].

assumption as well, that the galaxy cluster is spherical symmetric [3]. This assumption could be invalid in all the same cases as for HSE described above, as they would perturb perfect symmetry. It is also worth noting that the error due to these assumptions is even greater at higher redshifts, where mergers were more frequent [16]. That being said, X-ray mass estimates of galaxy clusters are not prone to a large underlying systematic error [14, pp. 16–17]. Some studies have found that the HSE assumption is accurate to within $\sim 10\%$ [14], and that X-ray methods overestimate the cluster mass by about 5–10% on average [17].[9]

Aside: The Sunyaev-Zeldovich Effect Another primary method for estimating the mass of galaxy clusters is through the observation of the Sunyaev-Zeldovich Effect (SZ). The SZ is the upscattering of the cosmic microwave background (CMB) due to interactions with the ICM [6]. As the CMB photons pass through the ICM's gas, they will occasionally (very rarely) inverse Compton scatter off a free electron, gaining energy and shifting the CMB spectrum slightly [3]. The resulting average increase in the CMB's energy is dependent on both temperature and density of the ICM gas, and can therefore be used to recover the mass of the cluster. (Note that although the scattered photons will no longer travel along our line of sight, statistically speaking another photon will be scattered opposingly *into* our line of sight. Thus, the SZ does not alter the number of observed CMB photons, only their energy spectra.) [2]

2.3 Gravitational Lensing

Gravitational lensing offers a unique tool for probing the mass distributions of galaxy clusters. In contrast to the methods outlined in the previous sections, gravitational lensing does not rely on any assumptions about the baryonic physics or dynamical state of clusters [2, 6, 7]. Lensing can therefore theoretically yield more unbiased mass estimates [1]. Before we discuss the observables of weak gravitational lensing, we first review the fundamental mathematics of gravitational lensing.[10]

Gravitational lensing was first formally proposed by Albert Einstein in his theory of general relativity in 1915. In his description, massive objects distort the curvature of space itself, bending the trajectory of anything that passes by it, including light. Light travels through space along null geodesics, and if a massive object is located along its path, its path will be redirected by a certain angle. This *deflection angle* is a function of the mass of the lens and the impact parameter distance between the light and lens:

$$\hat{\alpha}(\xi) = \frac{4GM}{c^2\xi} \ , \tag{6}$$

where G is the gravitational constant, M is the mass of the object doing the lensing, c is the speed

[9] There is also bias in the collection of sample clusters from X-ray observations [6]. For example, "up to 20% of weak-lensing clusters have not yet heated their ICM to a level detectable with current X-ray missions" [18]. Thus, survey samples were created from clusters that were themselves detected via gravitational lensing [8].

[10] For a brief qualitative review of gravitational lensing, see Joanne D Cohn's (University of California, Berkeley) Gravitational Lensing.

of light, and ξ is the impact parameter [2, 6, 7, 19]. A diagram of the geometry of this deflection is shown in Figure 3.

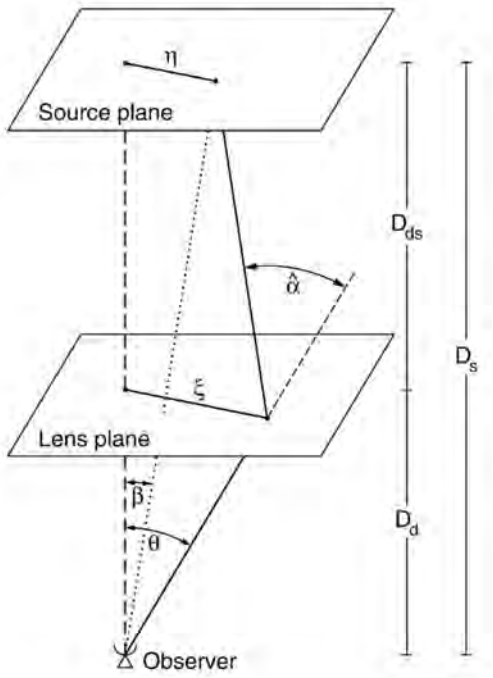

Figure 3. Simplified diagram of gravitational lensing geometry, under the thin lens approximation. *Source:* [19, p. 327]

In this diagram, the mass is located in the "Lens plane" at the point along the vertically straight thick dashed line. This assumption that the mass is entirely located within a plane is called the "thin lens approximation" and it is accurate to $\sim 0.1\%$ [2, 7]. In our study of galaxy clusters, this is a valid assumption because the actual depth of the cluster is much smaller than the distances from the observer to the lens (D_d) and from the lens to the background sources (D_{ds}).[11] The distance from the observer to the source is labelled D_s. It should be noted that all of these distances are angular distances [1, 16]. The thin lens approximation also implies that the light's trajectory is smoothly bent by the one deflection angle [19]. The source emitting the light is in reality located in the "Source plane" at the point along the dotted line. If no lens were present, we would observe the source to be at an angle β corresponding to a vector η from where the lens would be projected onto the source plane. However, if a lens is present, the source actually at an angle β, will instead appear at an angle θ. The source therefore appears at the point in the lens plane along the solid/small dashed line, with the impact parameter, ξ, being the vector between the mass and the source's projection onto the lens plane. The *lens equation* describes this behavior [2, 7, 19]:

[11] Here the subscript d stands for the "deflector"—it is also common convention to use l for the "lens" instead.

$$\begin{aligned}\beta &= \theta - \frac{D_{ds}}{D_s}\hat{\alpha}(\xi) \\ &= \theta - \frac{D_{ds}}{D_s}\hat{\alpha}(D_d\theta) \qquad \text{(using } \eta = D_s\beta,\ \xi = D_d\theta \text{ [19])} \\ &= \theta - \alpha(\theta) \qquad \text{(where } \alpha(\theta) = \frac{D_{ds}}{D_s}\hat{\alpha}(D_d\theta)\text{),} \quad (7)\end{aligned}$$

where in the second line, we make a transformation into angular coordinates, applying the trigonometric small angle approximation. In the third line, we explicitly define the scaled deflection angle, $\alpha(\theta)$. If there are multiple solutions to equation (7), an additional image will be visible at each θ that satisfies the lens equation [19].

The above explanation describes the case where the massive lens is a point source, but as we saw in Section 1, galaxy clusters are far from singular point masses. To expand the lens equation into 2-dimensions (only two, because we are still making the thin lens approximation that the cluster's depth is relatively small), we use the surface mass density, $\Sigma(\xi)$, instead of just the mass. It is defined as the 2-dimensional projection of the mass density onto the flat lens plane:

$$\Sigma(\xi) \equiv \int_{-\infty}^{\infty} \rho(\xi, r)\, dr \ , \tag{8}$$

where r is the coordinate along the line of sight and ρ is the 3-dimensional density of the lens (keep in mind that ξ is a 2-dimensional vector) [7, p. 14]. Therefore, the deflection angle for a thin, compact continuous lensing mass becomes:

$$\hat{\alpha}(\xi) = \frac{4G}{c^2} \int \Sigma(\xi') \frac{\xi - \xi'}{|\xi - \xi'|^2}\, d^2\xi' \ , \tag{9}$$

where ξ' is a dummy variable [19, p. 328]. If one uses the same angular coordinates transformation from Equation (7b) ($\eta = D_s\beta$, $\xi = D_d\theta$), the *scaled* deflection angle can be written as:

$$\alpha(\theta) = \frac{1}{\pi} \int_{\mathbb{R}^2} \kappa(\theta') \frac{\theta - \theta'}{|\theta - \theta'|^2}\, d^2\theta' \ , \tag{10}$$

where θ' is another dummy variable [19, p. 329]. Here, we have introduced $\kappa(\theta)$, the dimensionless surface mass density [1, 6, 7, 16, 19]:

$$\kappa = \frac{\Sigma}{\Sigma_{crit}} \quad \text{where} \quad \Sigma_{crit} = \frac{c^2}{4\pi G} \frac{D_s}{D_d D_{ds}} \ . \tag{11}$$

(Note that we hereafter drop κ's $D_d\theta$ (or ξ) dependence for simplicity.) κ is a key gravitational lensing property known as the *convergence*. It can be defined as follows:

$$\kappa \equiv \frac{1}{2}\nabla^2\psi(\theta) = \frac{1}{2}(\psi_{11} + \psi_{22}) \ , \tag{12}$$

where $\psi(\theta)$ is the 2-dimensional gravitational potential of the lens [1, 19].

Convergence represents the isotropic magnification of background sources, one type of effect that gravitational lensing produces [1, 6, 16]. In this case, the surface brightness does not change, as the number of photons is conserved, but the observed flux does change, as the solid angle that the light subtends changes [19]. This is because packets of light rays experience differential deflection, in which rays that are closer to the lens get deflected more so than those that are farther [2].

The other effect that gravitational lensing produces is the anisotropic tangential stretching of background sources, called the *shear*. Shear is a complex quantity defined as follows:

$$\gamma_i = (\gamma \cos(2\phi),\ \gamma \sin(2\phi)) = \gamma e^{2i\phi} \ , \tag{13}$$

where ϕ is position angle encircling the lens [6, p. 3]. Thus, this distortion is curl-free, only stretching background sources tangentially around the lens [1, 16].

Together, the image distortion from the convergence and shear can be represented by the following Jacobian matrix:

$$\mathcal{A}(\theta) = \frac{\partial \beta}{\partial \theta} = \left(\delta_{ij} - \frac{\partial^2 \psi(\theta)}{\partial \theta_i \partial \theta_j}\right) = \begin{pmatrix} 1-\kappa-\gamma_1 & -\gamma_2 \\ -\gamma_2 & 1-\kappa+\gamma_1 \end{pmatrix} \ , \tag{14}$$

where δ_{ij} is the Kronecker delta function and the shear has been equivalently defined as follows [19, p. 329]:

$$\gamma \equiv \gamma_1 + i\gamma_2 \ ; \quad \gamma_1 = \frac{1}{2}(\psi_{11} - \psi_{22}) \ , \ \gamma_2 = \psi_{12} = \psi_{21} \ . \tag{15}$$

From Equation (14), we see that the convergence and shear are related by the inverse 2-dimension Laplacian of the gravitational potential [16]. Lastly, it can also be useful to define a quantity that contains both terms, called the *reduced shear* [1, 6, 7]:

$$g = 2\,\frac{\gamma}{1-\kappa} \ . \tag{16}$$

(Note that both including and excluding the factor of 2 out front are common conventions [6]; for consistency, we will hereafter include it.)

2.3.1 Weak Gravitational Lensing

The weak gravitational lensing (WL) regime is defined by $\kappa, \gamma \ll 1$ [1, 6, 7, 19]. While strong gravitational lensing ($\kappa, \gamma > 1$) produces dramatic luminous arcs, Einstein rings, and multiple images, it only occurs for galaxy clusters near the dense centers of very massive clusters. WL on the other hand, is caused by all galaxy clusters, including their less dense regions, and is thus more widely applicable (technically WL affects all images to some degree) [16]. However, WL is an extremely subtle effect to detect. The distortion of individual sources, coupled with their intrinsic ellipticities,

is generally not directly observable. The measurement of WL is therefore an inherently statistical effort, utilizing observations of many background sources to analyze the average distortion.

Recall that the scalar ellipticity of an object (background galaxy) is given by:

$$\epsilon = \frac{a^2 - b^2}{a^2 + b^2} \ , \tag{17}$$

where a and b are the semimajor and semiminor axes, respectively [6, p. 3]. The ellipticity of a galaxy can also be written in vector form as follows:

$$e_i = (\epsilon \cos(2\phi), \epsilon \sin(2\phi)) \equiv (e_+, e_\times) \ , \tag{18}$$

where ϕ is the angular position of the source around the lens or the "azimuthal" angle [1, pp. 1–2] ($\phi = \frac{1}{2}\tan^{-1}(\frac{e_\times}{e_+})$, [6, p. 13]). e_+ and $e_\times$ are the components of the ellipticity in the x-, y-axes and $y = \pm x$ directions, respectively [6, p. 3], as depicted in Figure 4.

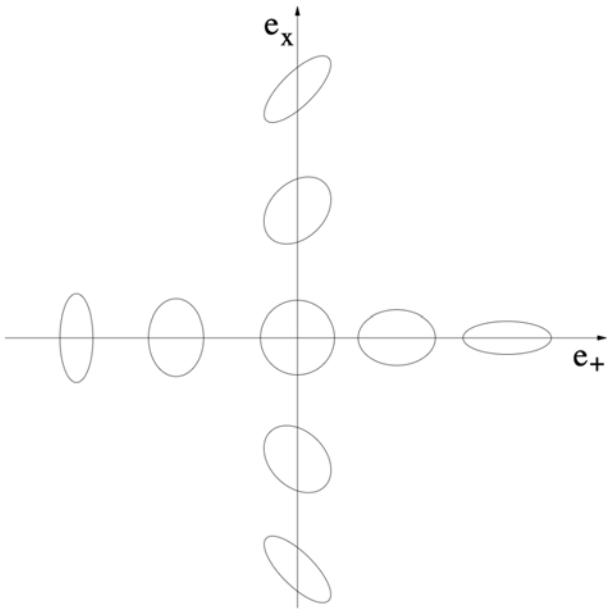

Figure 4. Tangential and cross ellipticity components of a source. *Source:* [6, p. 4]

These components are also known as the *tangential* and *cross* ellipticity terms, often written equivalently in terms of the polarization states of the complex ellipticity, e_1 and e_2, as follows [1]:

$$e_t = -\left(e_1 \cos(2\phi) + e_2 \sin(2\phi)\right) \ , \tag{19}$$

$$e_c = \left(e_2 \cos(2\phi) - e_1 \sin(2\phi)\right) \ . \tag{20}$$

The tangential component represents the "E-mode" statistic, analogous to the curl-free electric field in electromagnetism. The cross component represents the "B-mode" statistic, analogous to the divergence-free magnetic field. Rotating the E-mode through $\pi/4$ radians gives the B-mode,

but since gravitational lensing is curl-free, the B-mode should theoretically be zero for a symmetric cluster [16]. [1]

As described above in Section 2.3, the convergence produces an isotropic magnification. However, without prior knowledge of a source's inherent flux, κ cannot be directly measured [6, 16]. The shear also cannot be directly measured for a source, as the observed ellipticity is a combination of the intrinsic ellipticity (not known) and the reduced shear distortion: $\epsilon^I = \epsilon^S + g$, where the superscripts I and S represent the ellipticities in the image and source planes, respectively [2, 8]. Moreover, in the case of weak lensing, the distortion is dominated by the shapes of galaxies themselves [2]: "the intrinsic galaxy ellipticities are ~ 30 times larger than the distortions we are trying to measure" [16, p. 3]. The WL distortion is even smaller than the uncertainty of our galaxy shape measurements. Therefore, in order to measure the distortion, we must observe the shapes of many background sources to determine the average alignment and improve accuracy [16].

With no lens present, a sample of background galaxies is expected to have random orientations [2, 16]. For a large enough sample, the average intrinsic ellipticities should therefore cancel out to zero: $\langle \epsilon^S \rangle = 0$ [1, 6]. Thus, any observed alignment in the ellipticities of the background galaxies is assumed to be caused solely by the WL distortion. Substituting back in for the reduced shear, we get:

$$\langle \epsilon^I \rangle = 2\langle \frac{\gamma}{1-\kappa} \rangle \approx 2\langle \gamma \rangle \ , \tag{21}$$

where in the last step we use the fact that $\kappa \ll 1$ for WL [6, p. 4]. Furthermore, since $\epsilon = (e_+^2 + e_\times^2)^{\frac{1}{2}}$ [6, p. 13] and the average cross ellipticities also go to zero, and we are left with:

$$\langle e_t \rangle \approx 2\langle \gamma \rangle \ . \tag{22}$$

Therefore, the average tangential ellipticities of the background galaxies is an unbiased estimator of the WL shear [1, 16]. As mentioned above in Section 2.3, the shear can be used to obtain the convergence and reconstruct the surface mass density distribution of the cluster.[12]

The NFW Profile In order to estimate the mass of a cluster, a Navarro–Frenk–White (NFW) profile can be fit to the shear profile. First derived from N-body simulations in 1997 [20], the NFW profile describes the density distribution of relaxed dark matter (DM) halos (see Section 1) [2, 3, 7, 20]. In practice, it fits observational studies for clusters with masses between 10^9–$10^{15} M_\odot$ very well (encompassing most clusters of interest) [7, 21]. This profile makes the approximation that the virial radius is equivalent to the radius within where the mean overdensity of the cluster is 200 times the critical density at the cluster's redshift. The NFW profile is given by:[13]

$$\rho(r) = \frac{\rho_{crit}(z)\delta_c}{(\frac{r}{r_s})(1+\frac{r}{r_s})^2} \ , \tag{23}$$

[12] For a complete theoretical and mathematical review of WL, see [6] and [19], respectively.

[13] This profile is sometimes written with slightly different coefficient variables out front, but the result is the same.

where r_s is the scale radius [20, p. 3], $\rho_{crit}(z)$ is the "critical density for closure of the Universe at redshift z" [7, p. 17]: $\rho_{crit} \equiv \frac{3H^2(z)}{8\pi G}$ [20], and δ_c is the dimensionless characteristic density defined as follows:

$$\delta_c \equiv \frac{200}{3} \frac{c^3}{[\ln(1+c) - \frac{c}{1+c}]} \ . \tag{24}$$

Here, c is the concentration parameter, defined as $c \equiv \frac{r_{200}}{r_s}$ [21, p. 37], where r_{200} is the virial radius. Using the compressed 2-dimensional projection (thin lens approximation) [7, p. 30], the virial mass of the galaxy cluster can be estimated by:

$$M_{200} = 4\pi\rho_{crit}\delta_c r_s^3 \left[\ln(1+c) - \frac{c}{1+c}\right] \ . \tag{25}$$

Thus, based on the observed lensing curve computed from the tangential ellipticities, the NFW profile predicts the best-fit mass of a given cluster [22].[14]

3 Data

3.1 DECam

The images used for this research came from the wide-field Dark Energy Camera (DECam). This detector was designed to carry out the Dark Energy Survey (DES) Project and did so through the survey's completion in January 2019. DECam is mounted on the Victor M. Blanco 4-meter telescope at the Cerro Tololo Inter-American Observatory (CTIO), which sits atop a mountain in the Chilean Andes. Professor Dell'Antonio's lab has been using data from DECam for many years because its wide field of view (FOV) means that one can "image the entire virial region of a low-redshift cluster in a single pointing" [1, pg. 2]; it boasts a 2.2° diameter FOV, with a small pixel scale of 0.2637". Moreover, DECam was an ideal telescope for this research because its images should theoretically be deep enough to measure the WL signal through regions of fairly high extinction. DECam's detector is comprised of 62 charge-coupled devices (CCDs), each containing 2048×4096 pixels (at the time of writing, 60 CCDs remain fully operational—chips 2 and 31 are inactive).[15] Thus, the total resolution is 520 megapixels. A schematic of DECam's CCD configuration is shown in Figure 5a. [23, 24]

DECam has eight available filters (*u*, *g*, *r*, *i*, *z*, *Y*, *VR*, and *N964*) that range from 400nm to 1080nm [23, 24]. Generally, DECam is deepest in the r-band filter [16], and according to CTIO, "the VR filter is intended to be a 'discovery filter', not an 'accurate photometry' filter" [23]. Each of the wavelength bands associated with these filters can be visualized in Figure 6.

We retrieved DECam images from the NOIRLab Astro Data Archive, a database that provides open access to a diverse range of astronomical images from a variety of telescopes, including over five

[14] For a thorough mathematical review of the NFW profile, see [7, 20]

[15] Status reports of individual CCDs can be found at CTIO's Status of DECam CCDs

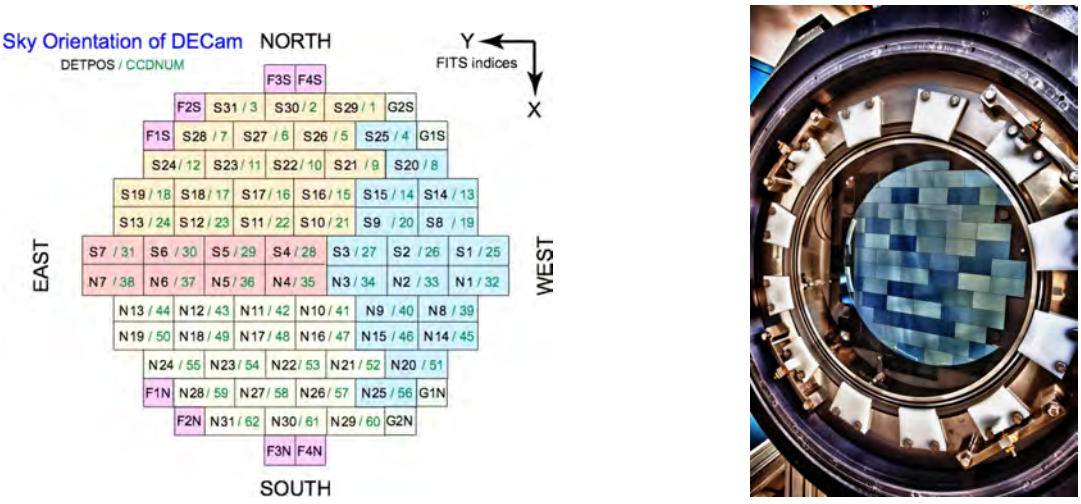

(a) Schematic of DECam's CCD configuration, with chips numbered in green. Note CCDs 2 and 31 were not active at the time of writing. *Source:* [24, p. 34]

(b) Image of the DECam detector; CCDs can be seen in blue. *Source:* DES

Figure 5. DECam CCD arrangements.

million DECam images. The archive has a web search interface that allows objects to be searched for by name or coordinates and for detailed filtering of results based on dozens of parameters. The specific search settings used in this study are discussed in Section 4.1.

3.2 RXCJ0524.4+0819

The high extinction galaxy cluster of interest for this study is RXCJ0524.4+0819. It is named by it's right ascension and declination (RA/Dec) coordinates on the celestial sphere, which equate to $\sim (81.115°, 8.329°)$.[16] RXCJ0524.4+0819's key properties are listed in Table 1 below. (Note that RXCJ0524.4+0819's redshift means that it also falls within the "nearby" low-redshift regime: $z \lesssim 0.10$ [1].)

RA	Dec	Redshift, z	L_{X500} (erg/s)	M_{X500} ($M_\odot$)
$05^h24^m27.5^s$	$+08°19'44''$	0.068	1.0626680×10^{44}	2.02560×10^{14}

Table 1. Properties of RXCJ0524.4+0819: right ascension, declination, redshift, X-ray luminosity, and X-ray mass (subscript 500 denotes calculations made for the radius within which the density is 500 times the critical density). Values from: [15].

Seeing as RXCJ0524.4+0819 is positioned only 8 degrees above the galactic plane, it is not surprising that it has a fairly high extinction. This cluster's extinction values in each of DECam's filters, as well as the approximate total exposure times available, are given in Table 2 below. As a result of its high extinction, RXCJ0524.4+0819 has not been as deeply observed as many other clusters and thus only has data available in the r, i, Y, and VR filters.

[16] An alternative name for this cluster is MCXC J0524.4+0819, although we will stay consistent with the 'RXCJ' labelling.

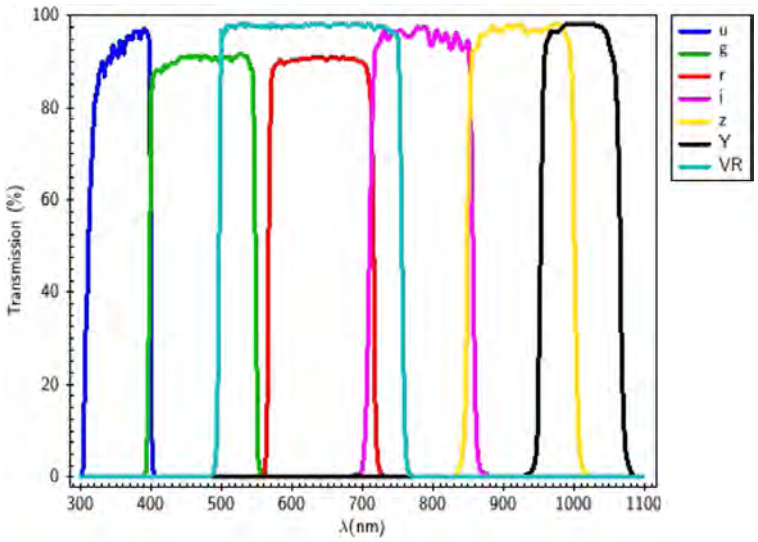

Figure 6. DECam's primary filter bands, with wavelength on the x-axis and transmission percentage (area weighted response) on the y-axis. *Source:* [23]

Measurement \ Filter	u	g	r	i	z	Y	VR
Extinction (magnitudes)	1.485	1.157	0.800	0.595	0.442	0.371	-
Exposure Time (s)	-	-	4000	900	-	900	1200

Table 2. RXCJ0524.4+0819's extinctions and observation times in each DECam filter.

In general, we want exposures to be both deep (large exposure time) enough to detect background objects clearly and taken in enough filters to be able to effectively separate galaxies from stars. That being said, the goal when selecting a cluster is to have $\sim$ 2000 seconds of exposure time in each filter and multiple filters with at least $\sim$ 1000 second exposure times. Aside from RXCJ0524.4+0819, the most promising candidates in our sample had only $\sim$ 1000–2000 seconds of exposure time total, often from just 2 filters.[17] This was the primary reason RXCJ0524.4+0819 was chosen for this study—it had the most observational data available, even though it lacked an ideal set of filters.[18] Moreover, RXCJ0524.4+0819 fit the cutoff used for "high extinction" of ~ 0.8 in the r-band, and had not yet had its WL signal measured and analyzed—this study is the first of its kind. It is also worth noting that this cluster did not have any CHANDRA X-ray Observatory images on the NASA/IPAC Extragalactic Database. Although X-ray data is desirable for overlaying X-ray contours onto the final image to study alignments, RXCJ0524.4+0819 still seemed to be the most approachable high extinction cluster in our database for the following WL study.

[17] A discussion of other high extinction clusters in consideration for this research can be found in Appendix B.

[18] One notable exception was the partially processed high extinction cluster RXCJ1407.8-5100, discussed in Appendix A.

4 Methodology

The bulk of the image processing in this study was done using a modified version of the LSST Science Pipelines[19], adapted for our group by Shenming Fu (for documentation on the LSST pipeline, see [25]). Many of these processes are computationally expensive and were run on the Brown University Center for Computation and Visualization's High-Performance Computer (Oscar) system. Intended for research use, this cluster features "more than 400 multi-core nodes, GPU nodes, and a high-performance parallel filesystem" [26] (for additional CCV specifications, see [26]). We also make use of the Astropy [27, 28], Astroquery [29], and Seaborn [30] Python packages at various points throughout the process.

Our image processing pipeline can be broken down into 5 stages:

1. Retrieving and Setting up Data (4.1)
2. Processing Individual Exposures (4.2)
3. Coadding Exposures (4.3)
4. Multi-Band Measurements (4.4)
5. Analyzing the Lensing Signal (4.5)

Each stage is further separated into individual steps with associated files of code for each procedure.

4.1 Retrieving and Setting up Data

The process begins with downloading raw data taken by DECam from the NOIRLab Astro Data Archive (see Section 3.1). As was discussed in Section 3.2, our cluster had images taken in the r-, i-, Y-, and VR-bands, with a range of exposure times. By design, the pipeline automatically goes to the archive, searches for the data using the cluster's name and coordinates, and downloads all images that are within a $4^\circ \times 4^\circ$ window around the cluster's center coordinates [22]. However, for some reason this function was unable to properly link with our cluster's coordinates, so the download process was done manually. To search for RXCJ0524.4+0819's images on the archive's web search, the cluster's name was entered to fetch its RA/Dec. The *radius* was set to a value of 3 which is larger than needed at this redshift, but ensures no potentially useful data is left out. The *process type* was set to "raw" and the *telescope & instrument* field was set to "ct4m, Decam". Lastly, we only used *exposures* greater than 25 seconds. Using the command line LFTP, the raw images were downloaded into their own subfolder within the cluster's directory.

After the raw images are downloaded, we ingest reference catalogs from other telescopes that contain photometric and astrometric information about some of the objects within the cluster's field

[19]The original pipeline is designed to process data for the upcoming Vera C. Rubin Observatory Legacy Survey of Space and Time (LSST), but it is easily applicable to other optical or near-infrared datasets [25].

of view. Photometry catalogs provide information on the brightness of objects and astrometry catalogs provide information on their positions. Specifically, we use catalogs from Gaia, Pan-STARRS1 (PS1), the Sloan Digital Sky Survey (SDSS), and SkyMapper (SM), that are in our database. For RXCJ0524.4+0819, because of its declination—in the northern hemisphere, just above the galactic plane—only Gaia and PS1 were used for astrometry and photometry, respectively.

In addition to raw exposures, calibration files need to be ingested in order to account for instrumental effects. These images include bias, flat, and fringe frames. Examples of a raw image along with each calibration image type can be seen in Figure 7. Bias frames, also known as "zeros", capture the intrinsic readout patterns of each of the CCDs. They have effectively zero exposure time and can therefore be thought of as images taken with the lens cap on. Having these exposures allows us to correct for inhomogeneities in the detector itself and produce more unbiased final images. Flat-fields (also known as "flats"), capture additional irregularities in the telescope's observation and are used to normalize pixel-to-pixel sensitivity [4, 22, 25]. Flat frames display imperfections on individual CCDs, due to dust grains on the device or other defects, inactive pixel columns, or inherent manufacturing imperfections. Figure 7c shows an example of a CCD that has both a column of "dead" pixels and a "tree-ring" pattern from the material used in the camera itself; these annular patterns are byproducts of how the silicon in the CCDs are manufactured, and must be corrected for to calibrate pixel sensitivity. Fringe frames capture the interference pattern that occurs when certain photons with long enough wavelengths pass through the detector, reflect off the back of the unit, and interfere with other incoming photons [4, 31]. An example of the resulting "wavy" pattern can be seen in Figure 7d. It is important to subtract off these fringe patterns in order to have consistent measurements across all CCDs.

With the raw data, reference catalogs, and calibration files retrieved, we then set up a data repository within the cluster's folder to properly link between each ingested file. Almost all of the image files we work with are of the type "Flexible Image Transport System" (FITS) or the tile-compressed version, FITS.fz.[20] Images of this type can be displayed using the SAOImageDS9 imaging application. Exposures are all labelled by *visit id* numbers that are identifiers for DECam itself and can be used to refer to specific exposures in future steps. A *_mapper* is used to "find and organize data in a format specific to each camera" [25]. The repository is also configured to enable *rerun chaining*, such that each new stage of steps outputs to a new rerun subfolder and modified runs preserve previous results [25]. The raw images are then ready to be processed.

4.2 Processing Individual Exposures

Once all of the raw images, reference catalogs, and calibration files have been properly ingested and organized, they are used collectively to perform data reduction and process the raw single-exposure

[20] More on the *.fits* file format here: https://fits.gsfc.nasa.gov/fits_documentation.html, and more on the *.fits.fz* file format here: http://archive1.dm.noao.edu/tutorials/fpack

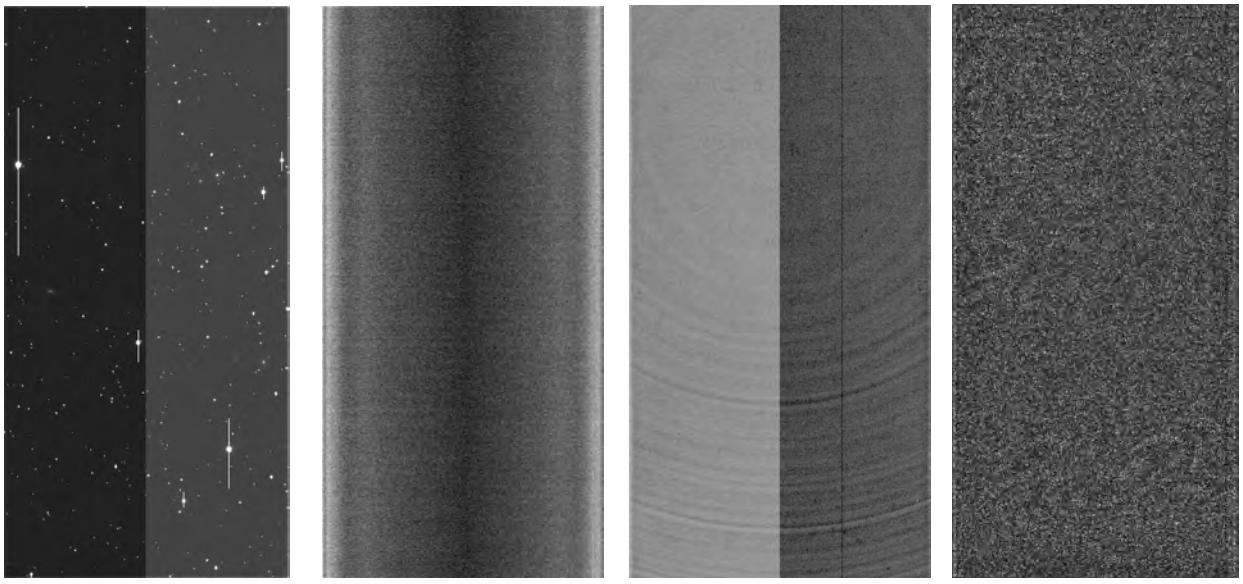

(a) Example raw exposure. *Visit:* 0707942, *Filter:* r, *Scale:* zscale-squared, *Date:* 12/19/2017

(b) Example bias ("zero") frame. *Scale:* zscale-linear, *Date:* 01/03/2020

(c) Example flat (sensitivity) frame. *Scale:* zscale-sqrt, *Date:* 03/16/2020

(d) Example fringe (reflections) frame. *Filter:* Y, *Scale:* zscale-squared, *Date:* 11/15/2013

Figure 7. Example raw and calibration images (bias, flat, fringe), each from one CCD. *Note:* images from different visits.

images. The first step is instrument signature removal (ISR), in which the effects of DECam itself are accounted for and subtracted out. This includes removing the detector noise and bias quantified by the bias frames. The flat and fringe frames are used to normalize the pixel-to-pixel sensitivity, adjusting for slight differences within each CCD chip. This process resulted in a fatal fringe correction error for the images in two of the Y-band directories. We decided to exclude the Y filter data from this point onwards, moving ahead with data from the r, i, and VR filters. Some dithering can also be applied to cover up gaps between CCDs [4]; dithering introduces low-level noise that smooths out emptier regions of the image. Additionally, bad pixels, such as the column shown in Figure 7c, are masked as they do not represent accurate readings and could cause issues down the road. Other types of unwanted objects are also masked, such as cosmic rays, bright stars, satellite trails, and asteroid trails [4]. These readings serve as foreground noise to the small lensing signal we wish to measure, and thus need to be identified. As Schneider describes, bright stars can cause "large diffraction spikes, and depending on the optics and the design of the camera, reflection rings, ghost images and other unwanted features" [4, p. 17].

The reference catalogs are then used to correct the sky coordinates and normalize the sensitivity of the images [22]. Astrometric calibrations set an initial World Coordinate System (WCS) for the images by referencing the positions of the objects in our astrometry catalog [25]. The WCS maps celestial RA/Dec coordinates to Cartesian pixel positions for astronomical images. Photometric calibrations set the zeropoint solution for the images by comparison with the brightnesses of the

objects in the reference catalog [25]. The photometric zeropoint solution is the apparent magnitude value that is equivalent to one count per second on the detector, and is used to determine the photometric relation between specific observations and standard magnitude measurements. Once calibrated, preliminary catalogs of the detected objects in each image are created.

The next step is to model the point spread functions (PSF) of the images, which describes how the camera responds to point sources. In this case, there is an additional effect induced by both the atmosphere ("smearing") and telescope itself ("shearing"). These effects are generally much more significant than the WL distortion and heavily obscure any signals we are interested in. It is therefore imperative that the PSF be corrected for in order to achieve accurate results. As is the case for ground-based telescopes such as DECam, atmospheric turbulence causes objects in the sky to appear more circular than they actually are, masking the WL's shear effect. This circularization is known as "atmospheric seeing" or "smearing" and it acts isotropically. It is also referred to as "broadening" as the shape of the resulting PSF curve is widened [8]. In contrast to the isotropic effect that the atmosphere has on the PSF that *dilutes* the WL signal, an anisotropic effect is introduced by the telescope that *mimics* the WL signal [16]. Telescopes do not usually perfectly resolve "point sources" such as stars (small focusing variations or tracking errors augment this); all objects are given some false ellipticity that affects the PSF. This effect is therefore referred to as "shearing", although it is innately distinct from the actual shearing due to WL (they are given the same name because the PSF effect mimics the WL effect).[21] For DECam, this effect is about 2–4% elliptical, which dominates the ellipticities induced by WL shearing. This effect is also more intense in the outer chips [16] and changes slightly over time as the telescope is used, so each CCD needs to be treated separately. [1, 6]

We model the PSF by looking at the previously cataloged detections and selecting a set of stars to examine for each image. The PSF manifests itself as the spatial variation of the sizes and shapes of stars [22]. Theoretically, these stars should appear perfectly circular with well-defined outlines, so measuring their PSFs is a logical way to model deviations from the predicted tight and narrow curve. Specifically, we use the HSM module's re-Gaussianization ("REGAUSS") method, originally devised by [32]. This involves fitting the stellar PSFs to Gaussian distributions and computing the full width at half maximum (FWHM) spread of the curve. To correct for the PSF, images can be convolved with a kernel of opposite ellipticities to the PSF [6].[22]

Having removed the instrumental signatures and defects, calibrated the sources, and modeled the PSF, the outputs of this processing step include calibrated exposures (*calexp*), background models (*bkgd*), and source catalogs (*src*). The outputs are organized by *visit id* number—there is one processed calibrated image for each CCD, with the background subtracted and a list of detected objects [7]. An example of the *calexp* and *bkgd* images for a single CCD is shown in Figure 8.

[21] Hence, all further mentions of "shearing" or "shear" will refer to the WL effect.
[22] For more on the effectiveness of PSF correction, see [4].

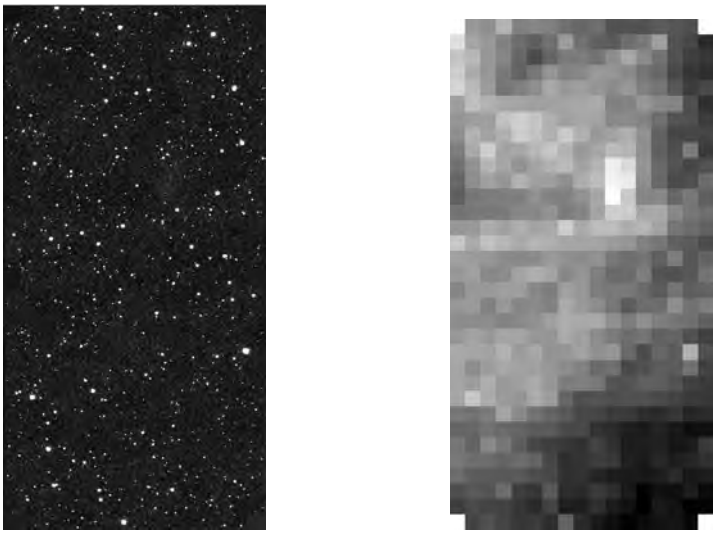

(a) Calibrated exposure (*calexp*). **(b)** Background model (*bkgd*).

Figure 8. Example outputs of processing a single-exposure - *Visit:* 0185445, *CCD:* 60. Relative image quality has improved compared to Figure 7a. Also, notice the alignment between bright stars/dust in the left image and the bright spots in the right image.

We then perform "checks" on each of the visits, for additional data reduction. Any CCDs that are located greater than 1.5° from the center of the cluster are removed. In addition, the PSF of certain images could be too distorted to be salvageable. Thus, images where the stars are either too elliptical (telescope issues) or too blurry (atmospheric seeing) are ignored [22]. We determine which images this is the case for by looking at the ellipticities and FWHM of the stars within each visit and CCD. Example output graphs of these features are shown in Figure 9. Figure 9a plots the ellipticities of the stars for a single visit in each CCD with their RA/Dec coordinates on the x-/y-axes. As previously mentioned, all stars should theoretically have $\epsilon = 0$, so the observed deviations from zero are good estimators of the PSF at different points in the FOV. This specific visit is a rather clean one in this regard, as most of the inner CCDs capture close to zero ellipticities. Only a few areas in the outer region of the image surpass the cutoff we use for measurements, ~ 1.2.[23] This makes sense, as most telescopes, including DECam, have slightly greater error in the edges of their FOV. Figure 9b plots the FWHM of the stars for the same single visit in each CCD with their RA/DEC coordinates on the x-/y-axes. This measures the width of the stars in pixels, essentially showing how blurry they are in different regions of the image. Again, stars should all theoretically have narrow PSFs that have well-defined borders with the surrounding image, so the observed FWHMs are good estimators of the PSF from atmospheric seeing at different points in the FOV. This specific visit is fairly clean in this regard as well, as most of the inner CCDs measure values of approximately 3.7–4.2. Only in the outermost chips, do the FWHMs approach the cutoff we use for measurements. In the r-filter, this value is ~ 4.5, and for other filters is much higher, nearing 7.0. This is still in agreement with the fact that DECam is expected to produce more

[23] We use a significantly higher cutoff value for general photometry.

error in the edges of its FOV. Lastly, Figure 9c plots the directions that individual ellipticities are pointing for this visit in each CCD with their RA/Dec coordinates on the x-/y-axes. If an overall directional correlation in the elliptical stretching of the stars is observed, it is likely an indication of a significant tracking error across many CCDs. In this visit, no such correlation can be seen, as the lines appear more like a collection of random dots.

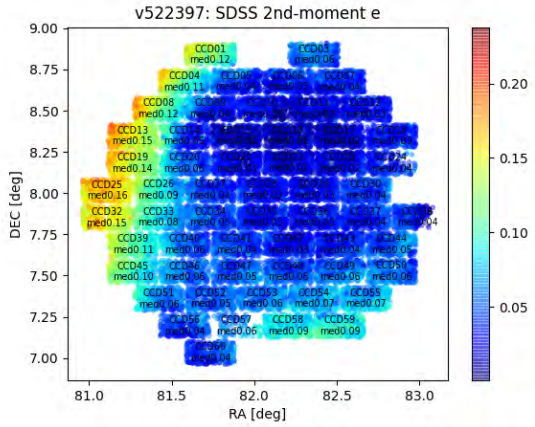

(a) Ellipticities of the stars in each CCD. The redder the region, the more elliptical the stars are.

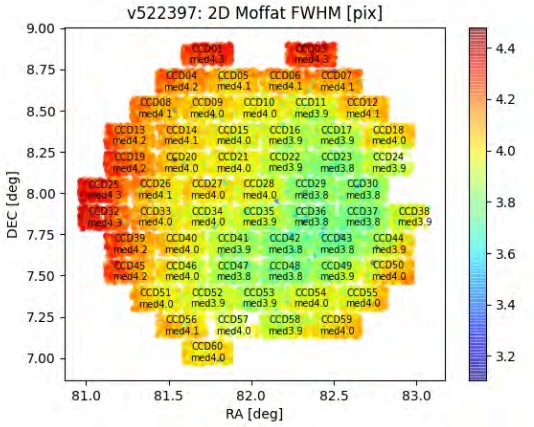

(b) FWHMs of the stars in each CCD. The redder the region, the blurrier the stars are.

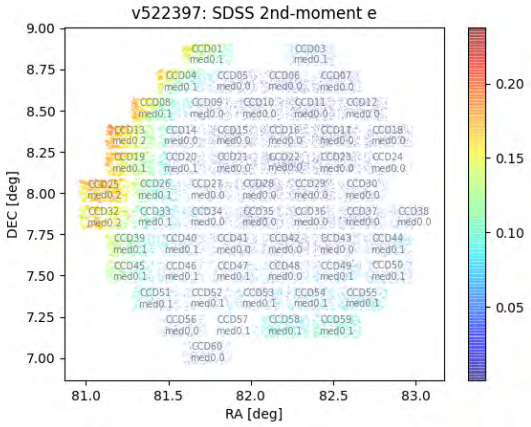

(c) Quivers of the stars in each CCD. If an alignment of the small line segments was observed, it would be indicative of a tracking error.

Figure 9. Example output images for manually checking a visit's PSF - *Visit:* 522397, *Filter:* VR

With the remaining calibrated exposures, a mosaic image is made of each *visit* for further manual examination of images or specific chips that might cause issues in future steps [22]. A list of successful visits and CCD numbers within those visits is also created. One of these mosaics, with a few problematic chips, is displayed in Figure 10.[24] First, any images that had fewer than seven CCD exposures are removed from the visit list (this includes empty visits), as their limited data

[24]Note that as mentioned in Section 3.1, chips 2 and 31 are no longer in use, and all visits have a slight distortion of vertical lines in CCD 57.

will cause the subsequent *joint calibration* step to fail. In this case, many visits were thrown out at this checkpoint. Second, any individual chips within the mosaics that look problematic are removed from the list of CCD numbers for that visit. These bad chips could be from large satellite trails, partially-defective CCDs, or other odd distortions. Multiple CCDs were tossed from nine additional visits, including those in Figure 10 that contain the satellite trail. Lastly, any remaining mosaics that appear to be otherwise defective or corrupted are removed—in this case, two additional images were thrown out that had a peculiar striped pattern.[25] By the end of this step, we have a refined list of successful visits and specific CCDs that will be used for the rest of the procedure [22].

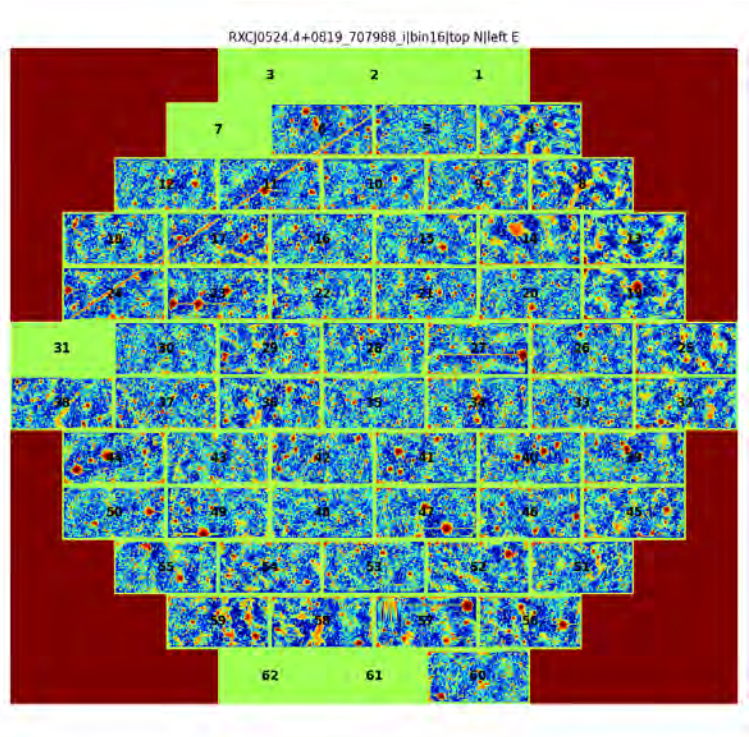

Figure 10. Example output image for manually checking a visit - *Visit:* 707988, *Filter:* i. Note the satellite trail that cuts through CCDs 6, 11, 17, 18, and 24. Red spots are bright stars.

4.3 Coadding Individual Exposures

Once the individual exposures are cleaned up and calibrated, we stack them together to improve the depth and signal-to-noise ratio (S/N)—a process known as coaddition. In order to do so, a unified WCS must first be established. This is done by generating a discrete "skymap" that divides the sky coordinates (RA/Dec) into grid of "patches" (pixels) and determines how the exposures will be laid out within these patches [7, 22]. As stated in the LSST Science Pipelines, "A sky map is a tiling of the celestial sphere, and is used as a coordinate system for the final coadded image" [25]. This nonlinear transformation [4] is valid because the small subsets of the celestial sphere

[25] As a general rule, all visits that begin with '21...' should be also be removed, although there were none for this cluster.

that we are observing can be approximated by flat overlapping rectangular regions, called "tracts" [25]. Our full FOV is mapped into one tract of patches ranging from (0,0)–(11,11), although in most cases we only use the patch ranges (5,5)–(6,6), (4,4)–(7,7), and (3,3)–(8,8) as windows into the central, middle, and outer ranges of our FOV, respectively.

Next, we perform a joint calibration (*jointcal*) of all the exposures for each patch, greatly improving the images' astrometry and photometry measurements [7, p. 77]. This step uses the original reference catalogs (Section 4.1) as well the new catalog of detections (Section 4.2) which provide information on significantly more sources in our images. For astrometric calibration, jointcal ensures that objects have the same positions in different exposures; it cross-correlates objects across exposures and solves for the transformation needed to maintain consistent positions [22]. For photometric calibration, jointcal makes sure that all objects are appropriately weighted between exposures. As outlined in [22], jointcal generates a model of the "absolute sensitivity as a function of position on the chips", and solves for scaling differences between exposures. The results are improved catalogs with objects in the same positions and consistent brightness weightings in each exposure, enabling them to be stacked correctly. It is worth noting that this step produced "negative scaling" errors when run on the r-band and i-band. In order to debug these issues, additional visits needed to be removed from the lists created in Section 4.2. Ignoring visits using the r and i filters that had 10 or fewer CCD exposures solved this error and allowed jointcal to run fully.

The re-calibrated exposures are then warped into the WCS of the skymap, a necessary step before full coaddition. Which patch each exposure will coadd into is determined, and the exposures are distorted accordingly so that they will all align properly in their respective patches [22]. The resulting semi-coadded images are called "temporary exposures" (*TempExp*). We also filter out any exposures that do not fit on a patch [25].

The gridded patches of warped exposures are assembled together to create deep coadded images with greatly increased depth and S/N [25]. To do so, a weighted average is constructed for each patch, of the signal that each of its input CCDs contribute to each pixel. In an analogous manner, a weighted average of the PSF is calculated for each patch [22]. We now have a single coadded image (see Figure 11) for each filter (i, r, VR) and patch range (i.e. central, middle, outer). The higher quality of these images mean that they will yield better shape and flux measurements (Section 4.4).

At this point, after removing problematic exposures at various points in the process, the following number of visits remain for each band: r–10; i–13; VR–13. Ideally, upwards of 20–30 visits are desired for each filter. This is especially true for r, whose coadded image is missing significant chunks. The limited amount of data remaining is a reflection of primarily the overall low exposure times for this cluster as well as dust extinction likely causing some exposures to be unusable. However, as we will see in Section 5, we are still able to attain accurate results from this data.

Figure 11. Stacked coadded image for the i-filter and middle range ((4,4)–(7,7)). Note the improved depth and S/N. RXCJ0524.4+0819's BCG can be seen in the center of the frame.

4.3.1 Combining Filters into Color Optical Image

In this step, we use the previously coadded optical images to create a deep composite color image. Three stacked images from the available filters can be chosen as our red (R), green (G), and blue (B) colors, and combined together to construct a color picture. For RXCJ0524.4+0819, because of the significant gaps in the r-band image, our final optical images were generated using only two of the filters: i and VR. The *.png* image of the central region produced using the i, VR, and i filters as R, G, and B, respectively, is shown in Figure 12. RXCJ0524.4+0819's elliptical brightest cluster galaxy (BCG) can be seen just to the left of the cluster's center, along with other surrounding galaxies. The hazy cloud-like filaments throughout the image are caused by the foreground galactic plane dust—a visualization of the challenge that comes with studying high extinction clusters. The small discolored rectangular regions in the bottom right of the image are artifacts from regions with missing or distorted data, and the straight lines scattered throughout are additional artifacts from bright stars. Alternative color combinations are presented in Appendix C.1.

4.4 Multi-Band Measurements

Now that the individual exposures have been coadded into deep stacked images, we build a new joint catalog of sources. These measurements will yield more accurate results than before, as the coadded patches have greater depth and S/N. The first two steps are to detect the sources in each

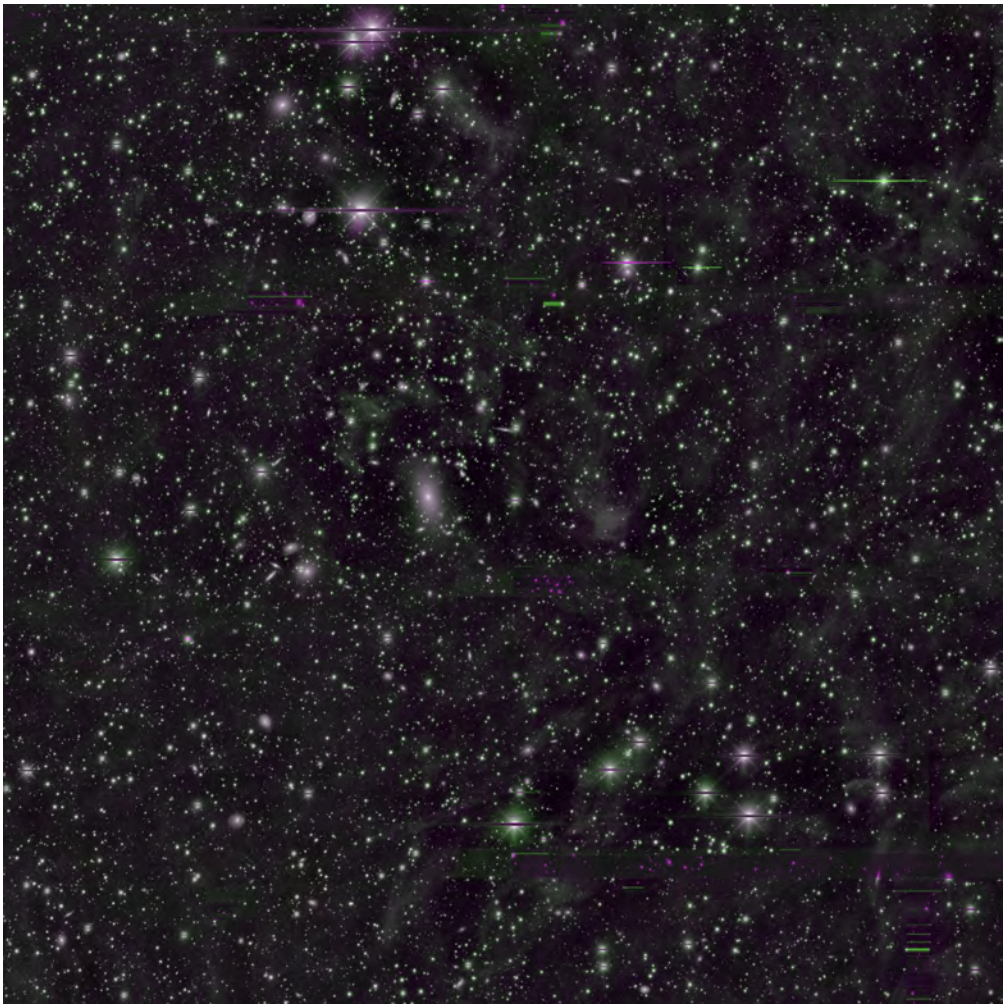

Figure 12. Composite optical color image for the central region ((5,5)–(6,6)) using the i/VR/i filters. The hazy green filaments are from the dust along our line of sight. The rectangular purple regions in the bottom right and above the the BCG are artifacts.

combined image and merge the catalogs from every filter. We also measure both the combined weighted sum of contributing PSFs and the S/N. These source catalogs are combined for every filter into a merged list for each patch. Sources in the catalogs are then *deblended*. The previous program may have detected overlapping sources as individual objects when in fact they are two separate ones. Deblending splits these overlapping sources into their corresponding child peaks, determining which pixels belong to which object. Each of the sources in the joint catalogs is then measured, including their sizes, shapes, and PSF-corrected ellipticities. Using this information, the objects are marked as to whether they are galaxies or stars. This is important because we only want to measure the ellipticities of the background galaxies, not the circular foreground stars. As these measurements are merged, we determine which filter best measured each source's position. This is called the "reference filter" and it can be different for different sources. We then re-measure the photometry of each object in all filters using the size and position information in the reference filter—a technique called *forced photometry*. This method of measuring individual sources at a

fixed position across filters, results in more accurate photometry. [22, 25]

When first running this stage of the process, errors were encountered in the VR-band. By removing the two visits in this filter with the fewest active number of CCD chips (23 each) and rerunning back from the *skymap* step, the issue was fixed.[26] The resulting number of remaining visits is already reflected in the discussion at the end of Section 4.3. Additional errors were raised in multiple filters, but they only occurred in the outermost edge patches of the image (near patch 0 or 11). They were therefore ignored as the regions fell outside the area in which we were most interested.

4.5 Analyzing the Lensing Signal

Finally, with accurate catalogs for each filter of all of the sources in our images, the WL signal can be analyzed. We create convergence maps of the density distribution, overlay them on the optical image, plot the shear as a function of radius, and use this profile to estimate RXCJ0524.4+0819's mass.

First, the deepest filter is chosen, to be used for analysis of source measurements. The others are used for additional color information. Usually, the r-band is chosen as it is inherently the deepest filter for DECam as mentioned in Section 3.1. However, because of the issues caused by limited r-band data making it through the pipeline (see Section 4.3), the i-band was chosen as RXCJ0524.4+0819's deepest filter for studying the WL signal. The i filter is often the second choice for DECam analyses, so this switch is not concerning. Second, the i-band's detailed source catalogs (*.fits* format) are extracted out into *.fiat* and *.csv* formats to be readable in the subsequent lensing analysis step [22]. Note that we run an additional optional cataloging step called *read_merge_full_catalog*. This is simply to compile a complete non fiat-format catalog for potential future use in contexts other than WL. Both of these steps are done for the different sets of patch ranges detailed in Section 4.3.

A map of RXCJ0524.4+0819's surface mass density can be reconstructed using the measurements gathered in Section 4.4. This provides a visual depiction of which areas of the cluster have relatively higher concentrations of mass. Seeing as galaxy clusters are generally $\gtrsim 80\%$ DM, this image maps the distribution of DM in the cluster. As described in Section 2.3.1, the converge is equivalent to the dimensionless surface mass density of the lens (Equation (11)). (Technically, convergence is the surface mass *over*density, as it is the ratio of Σ to Σ_{crit}, but for simplicity we will use the two terms interchangeably.) In other words, the map of the surface (over)density is also a map of the WL convergence. The convergence is related to the observed WL shear as they are both second derivatives of the gravitational potential (see Section 2.3.1) [7, 21]. Since the average ob-

[26] This somewhat higher than the usual minimum number of CCDs required for calibration and cataloging ($\lesssim$ 7–11). This could potentially be a result of a limited number of detectable sources in those specific visits.

served ellipticities of the background objects is an unbiased estimator of the shear (Equation (21)), we have everything needed to produce a visual map of RXCJ0524.4+0819's mass distribution.

In order to create the convergence map, we examine correlations in the ellipticities of the background galaxies in our images. To perform this task a program called *fiatmap* is run, which looks at how tangentially oriented the ellipticities of all galaxies in catalog are about one pixel. It repeats that process for every pixel in our image, taking into account each pair of sources' distances, in order to map how significantly each pixel in the FOV is distorting the background sources. This represents the areas of highest relative surface mass density and directly maps the distribution of matter in the cluster; points around which background galaxies are more tangentially sheared indicate local higher masses. The convergence map for the middle range of our image is presented in Figure 13. Figure 13a on the left is for the E-mode or tangential ellipticities (see Section 2.3.1). It depicts the areas of mass overdensity as lighter regions and less dense areas of mass as darker regions. Figure 13b on the right is for the B-mode or cross ellipticities. As explained in Section 2.3.1, these values should theoretically be zero everywhere as there should be no overall preferred orientation of the cross ellipticities. In practice, because we are only looking at a finite region of space and there is systematic error and noise in all of our measurements, some B-mode signal is still observed. Nonetheless, the values of the B-mode peaks are roughly an order of magnitude lesser than the peak values in the E-mode figure.

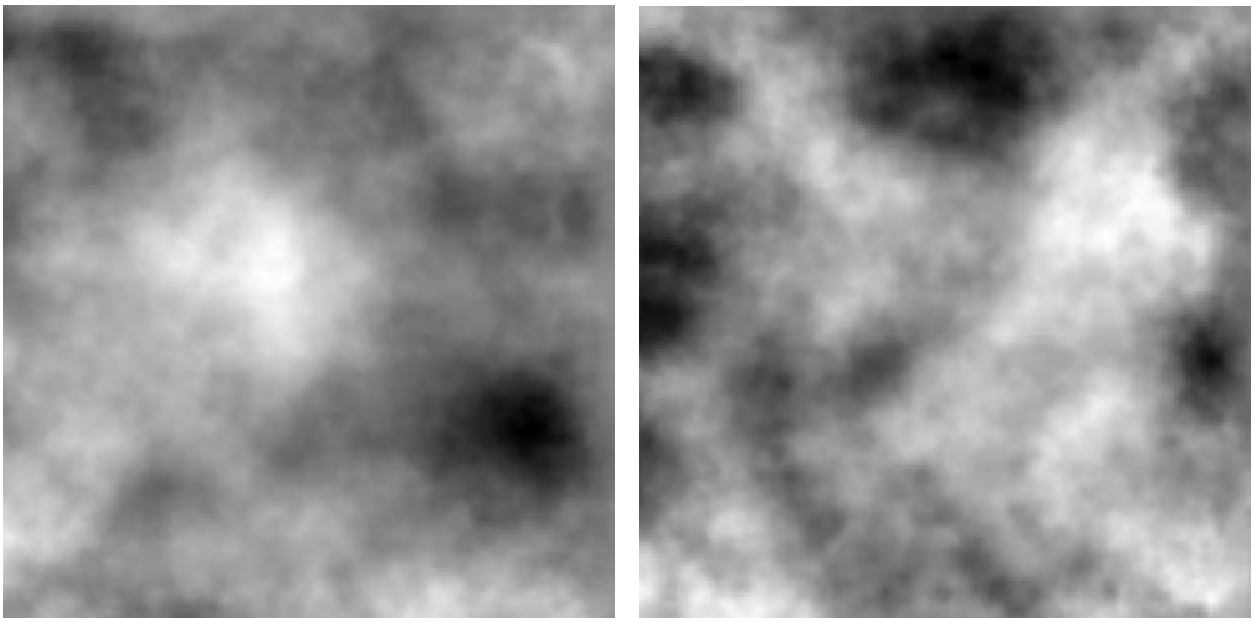

(a) E-mode signal (tangential ellipticities). Shows a matter density peak to the upper left of the center of the frame in white. Darker regions reflect mass underdensities.

(b) B-mode signal (cross ellipticities). Can be used as a statistical control.

Figure 13. Surface mass overdensity/convergence maps for the middle range ((4,4)–(7,7)). The peaks in the E-mode are about an order of magnitude greater than the peaks in the B-mode.

It is even more useful to have a coordinate system visually paired with these convergence maps. We therefore plot the contours of these maps as an overlay on top of the color optical images generated in Section 4.3.1, using the already established WCS. It is also common practice to overlay contours of the X-ray distribution using images from telescopes such as the CHANDRA X-ray Observatory. However, as mentioned in Section 3.2, when searching on the NASA/IPAC Extragalactic Database for CHANDRA data, no images were found for RXCJ0524.4+0819; its surveys likely avoided this cluster because of its proximity to the galactic plane (i.e. high extinction). We also looked for images from older X-ray telescopes such as ROSAT and Einstein Observatory. Although RXCJ0524.4+0819 was detected by ROSAT, these images are generally not high enough resolution to be useful when plotting contours. For these reasons, the final results for this cluster do not include an X-ray contour overlay, only the surface mass density map overlay. These overlay images allow for direct inspection of the morphological correspondence between the galaxies themselves, the mass (DM) peaks, and when available, the hot X-ray emitting gas [22]; their alignment or lack thereof is of great relevance to astrophysical and cosmological models. The final overlay image is presented in Section 5.1.

In addition to being used to deduce the convergence, the WL shear can be studied itself. We construct plots of the tangential ellipticities (shear) and cross ellipticities (statistical control) as a function of radius. This is achieved by dividing the catalogs of background galaxies into annular bins around the center of the cluster and calculating the mean tangential ellipticity (and cross ellipticities) for each bin. By plotting the average ellipticities at increasing distances from the cluster's center, we get the intensity of the WL signal as a function of radius. We then fit a NFW profile (see Section 2.3.1) to the shear curve to estimate the cluster's mass. These fitted profiles are presented in Section 5.2.1.

For this analysis, a center point must be chosen around which to annularly measure the shear. By default, the program uses the coordinates of the cluster's center as given by the database. However, when using this value for our analysis there was a significant alignment issue, leading to empty bins and a strongly negative shear in the center of the cluster. Instead, we chose to use the coordinates of the peak pixel in the convergence map as the center to evaluate the shear with respect to. One could argue that this is a more precise localization of the cluster's center of mass (assuming the error in our analysis is small). Therefore, slightly different values were used for each patch range the program was run on, as their maps' peaks varied slightly. These small changes of $\sim 0.03°$–$0.06°$ in RA and $\sim 0.1°$ in Dec made a significant difference in the lensing analysis and produced far better results. This alignment is crucial for getting accurate mass measurements [6]; as McCleary states, "the ambiguity in what is reported as the center of a WL peak can bias mass estimates through mis-centering of the tangential ellipticity signal" [1, p. 9].

We also need to provide information on the distances between the observer, lens, and background objects. As Wittman states: "a map of κ is not a map of mass. κ can be converted to mass only with a careful calibration of the source redshifts" [6, p. 23]. Only the redshifts, z, of each

of the background sources is needed since the cluster's redshift is already known and assumed to be constant (thin lens approximation, see Section 2.3). Although photometric redshifts are known for the background sources of some galaxy clusters, they are more difficult to obtain for high extinction clusters because of observational challenges. Hence, the redshifts of RXCJ0524.4+0819's background galaxies are unknown. To carry out the analysis, we assume all background galaxies to be at a redshift of $z = 0.6$. The implications of this assumption and the redshift requirement itself are further discussed in Sections 5.3 and 6.

Lastly, we employ a similar additional method for estimating the cluster's mass, called *global mass fit*. This process takes subsets of the source catalog and makes a shear profile like the one described above, but averages over all galaxies rather than bins of galaxies. It then plots the spread of estimated masses from those samples to produce a histogram of predicted mass values, with the mass on the x-axis and the density at which that value was estimated on the y-axis.[27] We make the same aforementioned assumptions for the cluster center and background redshift distribution. Usually this step is run on the patch ranges (5,5)–(6,6), (4,4)–(7,7), and (0,0)–(11,11). However, our outermost catalog was for (3,3)–(8,8) and patches (0,0) and (11,11) had previous errors for the merged measurements mentioned in Section 4.4. Therefore, we chose to run this fit on the patch range (3,3)–(8,8) instead of (0,0)–(11,11) as our outermost window. The mass fit histogram results are presented in Section 5.2.2.

5 Results and Analysis

In this section, we present the results of the procedure outlined in Section 4 for the high extinction galaxy cluster RXCJ0524.4+0819 (Section 3.2). We successfully measure the cluster's gravitational lensing signal and use those results to map the DM distribution and estimate the mass of the cluster.

5.1 Optical–Surface Density Map Overlay

In Section 4.5, we described how to create an overlay of the contours of the cluster's surface mass overdensity (convergence) map on the optical images generated in Section 4.3.1.[28] This was done for each set of FOV ranges (in patches), and for optical images created with multiple different configurations of filters. In Figure 14, we present the overlay image for the middle range ((4,4)–(7,7)). This was the widest region without significant distortions (for overlays of the innermost and outermost region ranges, see Appendix C.2). Here, the optical image is the one created from the i-band, VR-band, and i-band again, as this was the deepest combination of at least two distinct

[27] We use *seaborn*, [30], for this data visualization

[28] Ideally, one would also overlay the contours of the X-ray measurements, but as discussed in Sections 3.2 and 4.5, no X-ray images were available for this cluster.

filters (for different color schemes, see Appendix C). The x- and y-axes represent the RA and Dec coordinates, and the contours of the surface mass density/convergence map are shown in light blue. There appears to be an overall North-South alignment of the lensing signal in the inner regions, which does seem to match the alignment of the cluster's brightest galaxies. Furthermore, we can see that while the morphology of the lensing signal and optical image are relatively consistent with one another, there is a significant offset between the WL peak and RXCJ0524.4+0819's BCG. In other words, the DM distribution in the cluster does not appear to align exactly with the presumed optical distribution. Possible causes of this behavior are discussed in Section 5.3.

5.2 Mass Estimates from the Lensing Signal

As detailed in Sections 2.3.1 and 4.5, one can estimate the mass of a galaxy cluster by measuring the average tangential ellipticities of background galaxies and analyzing the resulting WL shear profile. The results of this procedure are presented and analyzed in the following subsections.

5.2.1 Shear Profiles

In Section 4.5, we described how to construct a profile of the WL shear as a function of radius and fit a NFW profile to it in order to get an approximate value for the mass of the cluster. Here, we present our findings. Figure 15 shows the shear profiles for each of the patch ranges (inner, middle, and outer) along with the theoretical parametric NFW fit. The x-axis is the radius from the center of the cluster in arcseconds and the y-axis is the average ellipticity of the background galaxies (divided by a factor of 2). The average tangential ellipticities are plotted in blue and depict the strength of the WL signal at each radius. The average cross ellipticities are plotted in orange and serve as a statistical control; as mentioned in Section 4.5 the cross ellipticities should theoretically average out to zero everywhere for a symmetric cluster, as the sample of galaxies will be randomly oriented and the shear is curl-free [1, 16]. Again, in practice this will usually not be the case, due to systematic error/noise, a limited number of sources, and possible asymmetries. In green, the best-fit NFW profile is plotted, corresponding to the cluster mass shown in the legend.

For the central range shown in Figure 15a, the shear profile cuts off before $\sim 2000''$ since the central region window only extends that far. In general, the NFW fit for this range is noticeably less accurate than for the wider ranges. As discussed in Section 4.5, there were difficulties getting a proper alignment of the center of the cluster, leading to the relatively low lensing signal at the smallest radii. There was a noticeably lower source density in this region, implying that there were fewer well-measured objects near the center of the cluster than expected. Moreover, there is significant noise at the largest radii for this range, as seen by the extended error bars. Due to these factors, the NFW fit yields a mass estimate of $1.0 \times 10^{15} M_{\odot}$—approximately 6–7 times greater than that of the middle and outer ranges. Although not ideal, this is not cause for serious concern, as we generally give more weight to the results from the wider ranges as they take into account significantly more sources and provide a more complete picture of the cluster's extent.

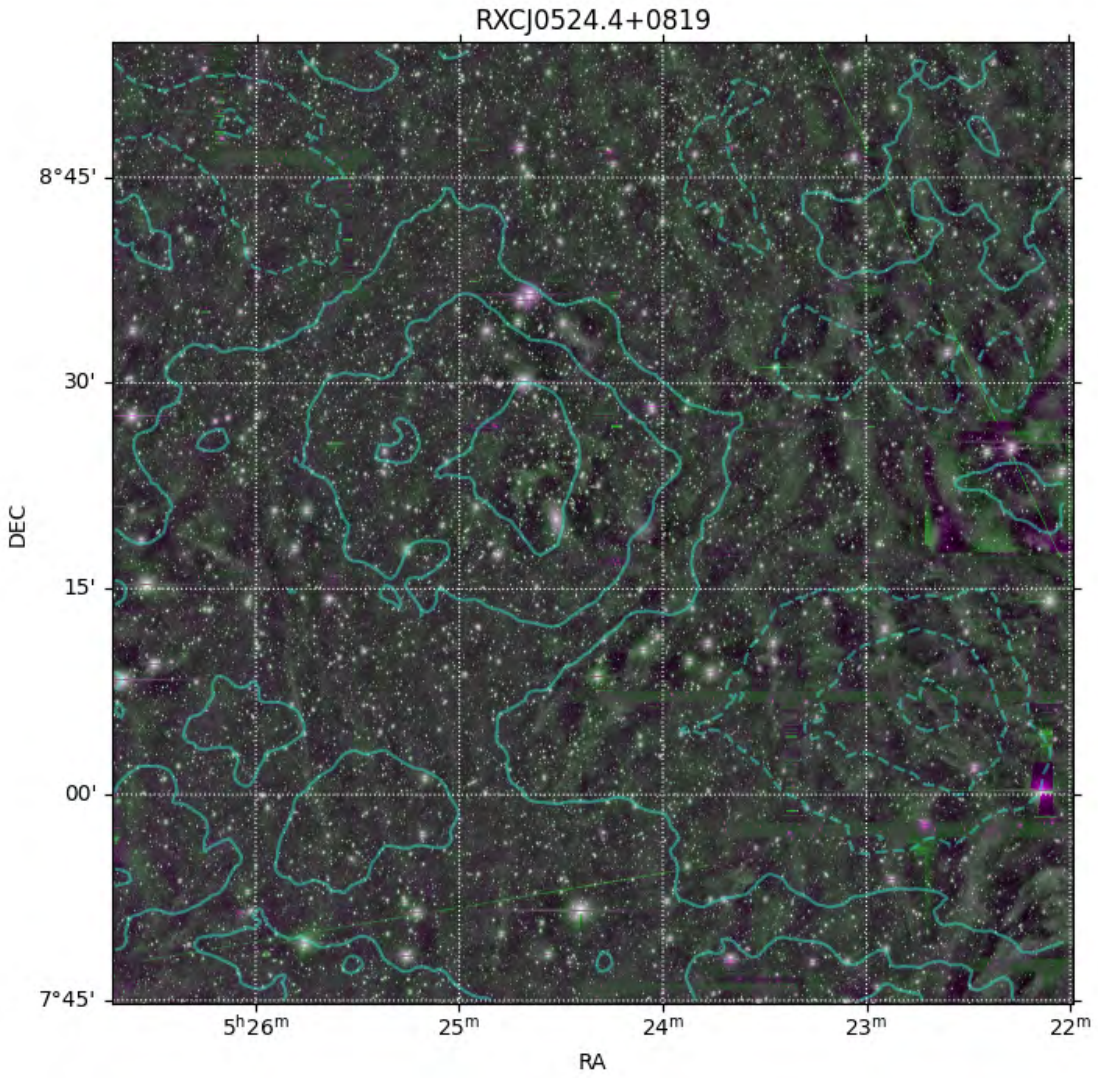

Figure 14. Overlay of the surface mass overdensity contours (in light blue) on the optical image (i/VR/i) for the middle range ((4,4)–(7,7)). Note the general agreement, but slight offset between RXCJ0524.4+0819's WL peak and BCG.

Encouragingly, the cross ellipticities for this narrow range all remain close to the expected value of zero, with a couple exceptions in the noisy outer radii.

For the middle range shown in Figure 15b, the profile follows a curve more expected of the WL shear (still not as well as the outer range). There is a more intense lensing signal at smaller radii that falls off at larger radii which is to be expected. Again, there is odd behavior at the largest radii. This is most likely a reflection of our images having more error at their edges and artifacts from incomplete stacking far from the cluster center. There is also relatively higher uncertainty at

the innermost radii due to noise. This is also expected, as there are simply fewer sources to measure the ellipticities of, at these smaller radii. The cross ellipticities are almost always significantly less than the tangential terms and near zero which matches the theory. The NFW fit yields a mass value of $1.5 \times 10^{14} M_{\odot}$.

For the outer range shown in Figure 15c, the shear profile follows the expected NFW profile very closely over all radii ranges. The WL signal is most intense near the center of the cluster and falls off as the distance from the center increases. In the innermost region, there is still a sizeable error, which is to be expected. As mentioned above, there are far fewer sources contributing to our estimates at these smaller radii, so these areas are anticipated to be noisier. Unlike in the previous cases, there is no additional unexpected spike in signal strength and error at the outermost radii. This could be explained by this range's clear FOV extending farther beyond the bounds of this plot's x-axis. The cross ellipticity terms are again always around zero and generally less than the tangential ellipticity terms. Here, the NFW fit estimates RXCJ0524.4+0819's mass to be $1.6 \times 10^{14} M_{\odot}$, which is in close agreement with the medium range and likely the most accurate value of the three.

5.2.2 Global Mass Fits

At the end of Section 4.5, we described a process for estimating RXCJ0524.4+0819's mass in a manner that is similar to, but slightly more accurate than the direct shear profile fits above. *Global mass fit* performs these shear fits for multiple subsets of the galaxies and graphs the distribution of predicted best-fit masses to select an average estimate. We present these final mass histogram results in Figure 16. Figure 16a shows the distribution of RXCJ0524.4+0819's best-fit mass for the narrowest central range and estimates an approximate cluster mass of $M_{200} = 1.74^{+1.00}_{-0.74} \times 10^{14} M_{\odot}$. Although still the outlier, this value is relatively more in line with the other two ranges than for the singular shear profile fits in Section 5.2.1. Figure 16b shows the distribution of the cluster's best-fit mass for the medium range and estimates an approximate cluster mass of $M_{200} = 1.61^{+0.70}_{-0.56} \times 10^{14} M_{\odot}$. Lastly, Figure 16c shows the distribution of the cluster's best-fit mass for the widest outer range and estimates an approximate cluster mass of $M_{200} = 1.66^{+0.71}_{-0.56} \times 10^{14} M_{\odot}$. As was the case for the shear profiles in Section 5.2.1, the results are most accurate for the outermost range ((3,3)–(8,8)). The centermost range has relatively inconclusive results, predicting masses as low as $\sim 0.5 \times 10^{14} M_{\odot}$ and as high as $\sim 3 \times 10^{14} M_{\odot}$, each over half as often as the average value. The middle range has a narrower spread, but still predicts lower masses fairly regularly. The outer range has the tightest distribution with the smoothest drop-off on either side of the peak. These results predict the mass of RXCJ0524.4+0819 with high significance. The mass likely falls between 1.0–2.5 $\times 10^{14} M_{\odot}$, with a best estimate of $M_{200} = 1.66^{+0.71}_{-0.56} \times 10^{14} M_{\odot}$.

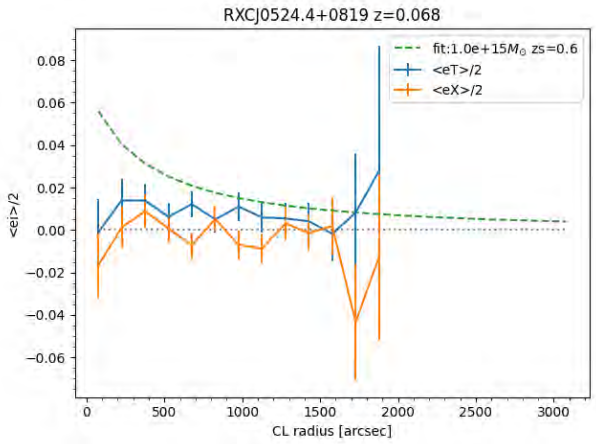

(a) WL signal as a function of radius for the inner range ((5,5)–(6,6)).

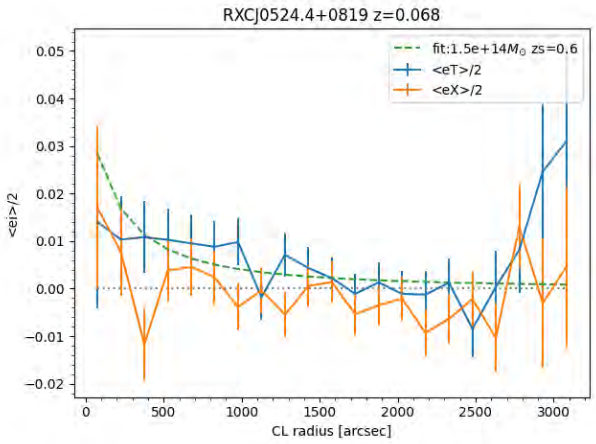

(b) WL signal as a function of radius for the middle range ((4,4)–(7,7)).

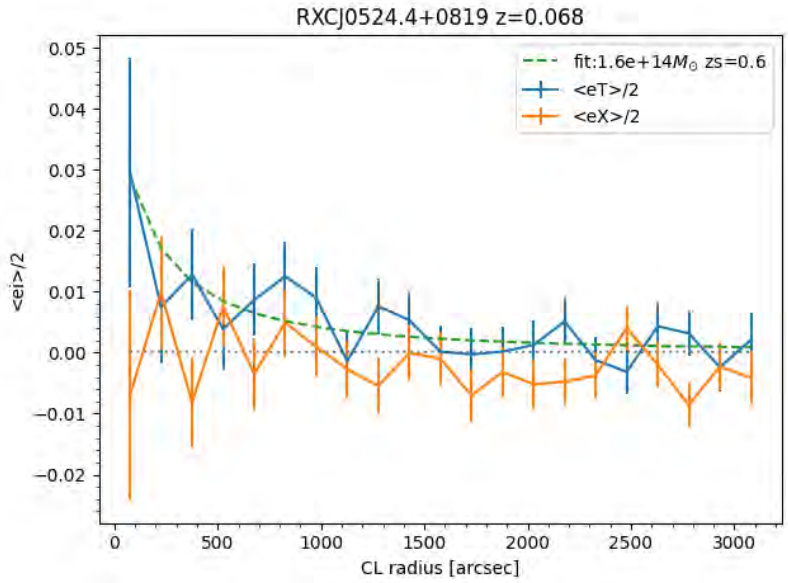

(c) WL signal as a function of radius for the outer range ((3,3)–(8,8)).

Figure 15. Fitted WL shear profiles as a function of radius for each region range. The average tangential ellipticity terms are plotted in blue with error bars. The average cross ellipticity terms are plotted in orange with error bars—these should theoretically be zero. The NFW fits are plotted in green, corresponding to the masses given in the legend.

5.3 Discussion

As alluded to in Section 5.1, there are a couple possible explanations for the offset between RXCJ0524.4+0819's WL peak and BCG displayed in Figure 14. First, RXCJ0524.4+0819 could be undergoing a merger with another galaxy cluster, causing its central galaxies and DM to diverge from equilibrium. Since DM only interacts gravitationally, one would expect the baryonic matter to "lag behind" the DM and thus the WL center.[29] Second, it is possible that RXCJ0524.4+0819's

[29]This phenomena can be visualized in CHANDRA's iconic image of the "Bullet Cluster", 1E 0657-56.

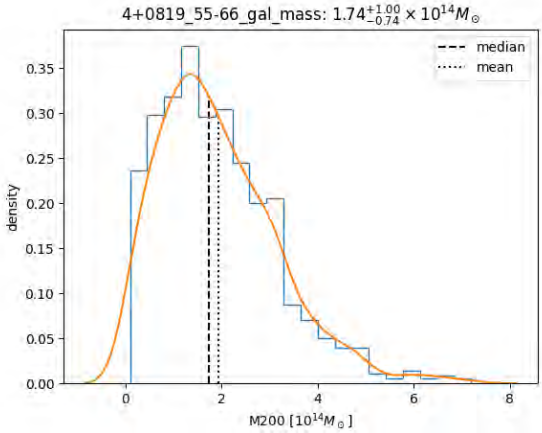

(a) Estimated mass histogram for the inner range ((5,5)–(6,6))

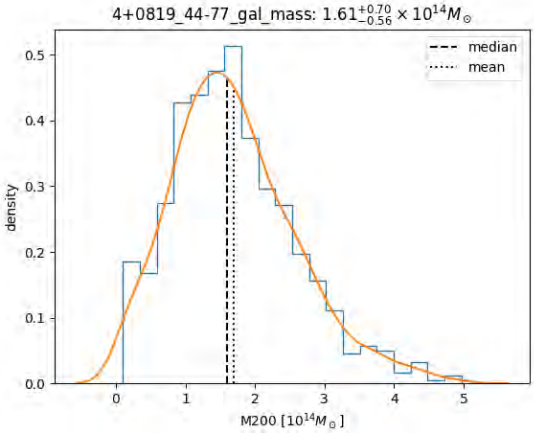

(b) Estimated mass histogram for the middle range ((4,4)–(7,7))

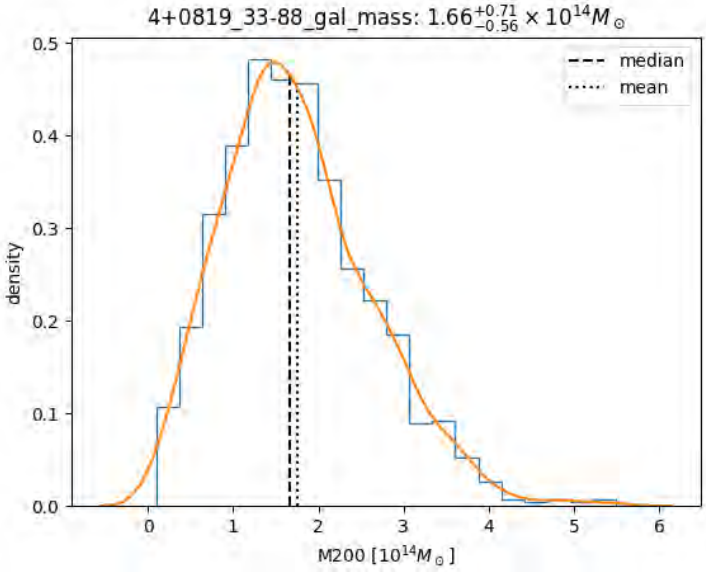

(c) Estimated mass histogram for the outer range ((3,3)–(8,8))

Figure 16. *Global* mass fit histograms for each region range. Estimated mass from the NFW fits are on the x-axis and densities at which that mass was predicted for each sample are on the y-axis. The orange curve is simply a visualization tool.

BCG is moving with respect to the cluster at some velocity and is not actually at the center. A further investigation of the dynamics of RXCJ0524.4+0819 would be needed to decipher the nature of this intriguing offset. It is also possible that the cluster's original center coordinate error was not completely fixed, and as a result the alignment is off. However, the offset does appear to be a genuine characteristic of the cluster given the accurate shear profile and mass fits for the widest patch range.

There also appear to be additional WL peaks in other areas of the image, particularly in the corners of the FOV. While these could theoretically correspond to other mass structures, it is much

more likely that they are a result of noise, increased error far from the cluster center, and the statistical look-elsewhere effect, which "guarantees that some high-significance peaks will appear regardless of the presence of any shear signal" [1, p. 12].

Comparing our mass estimates from Section 5.2 to the X-ray mass estimate given in Table 1 (Section 3.2), we find that they are consistent with one another; RXCJ0524.4+0819's estimated mass from X-ray measurements is $M_{X500} = 2.02560 \times 10^{14} M_{\odot}$ and our estimated mass from WL measurements is approximately $M_{200} = 1.66^{+0.71}_{-0.56} \times 10^{14} M_{\odot}$. Although consistent, note that these values correspond to masses that extend out to slightly different radii. The X-ray mass is measured out to a radius where the cluster's density is 500 times the critical density, whereas the WL mass is measured out to a radius where the cluster's density is 200 times the critical density. Therefore, the WL mass encompasses more of the cluster's virial region and should be slightly more accurate. It should also be generally larger than the X-ray mass, but in our study this is not the case.

In addition, there are other possible reasons for a disagreement between these two mass estimates. If the cluster is indeed experiencing a merger event with another cluster, it would be disturbed from hydrostatic equilibrium and yield inaccurate X-ray estimates [1]. Moreover, this could disrupt the spherical nature of the DM halos, meaning that RXCJ0524.4+0819 would not exactly follow a NFW profile fit [1]. Regardless, our assumption that the background galaxies are all at a redshift of $z = 0.6$ is a certain source of error in our final mass estimate. In reality, the background galaxies will be at a wide distribution of redshifts, so our exact mass value is most certainly inexact. That being said, this assumption is reasonably decent and will yield mass estimates similar to the X-ray estimates. Furthermore, this assumption is useful for comparing results from cluster to cluster. If we make the same assumption across a survey of clusters, their *relative* masses should generally hold, as the background redshift distribution will be random on average for different clusters. For example, if one cluster has a mass that is twice the mass of another and they use the same redshift assumption, their actual masses should have a ratio of approximately $2:1$. The observational data needed to determine the actual redshifts of background galaxies and attain more accurate mass measurements is discussed in Section 6.1.

In general, there are other sources of systematic error introduced throughout the procedure. These include instrumental effects (if not accounted for exactly), imperfect atmospheric correction of the PSF, heightened noise in the outer CCDs, imprecise background object shape measurements, amongst others. These small accumulating errors are in-part reflected in the convergence maps' non-zero B-modes and shear profiles' error bars. Finally, RXCJ0524.4+0819's high extinction was certainly a source of some error. It limited the number of exposures that could be successfully processed. For example, there were roughly 4000 seconds of exposure time in the r filter, but by the end of the process, only 10 visits could be used and there were significant gaps in the coadded image. For those exposures that did pass the criteria, extinction from dust introduced extra noise into the source measurements, affecting the measured lensing signal.

6 Conclusions

In this study, we successfully measured the weak lensing signal of the high extinction galaxy cluster RXCJ0524.4+0819 for the first time. From this signal, we mapped RXCJ0524.4+0819's dark matter distribution, overlaid it on our created optical image, and estimated the cluster's total mass. Our results were found to be consistent with the mass derived from X-ray observations. These findings are encouraging for the prospect of studying high extinction galaxy clusters through weak lensing.

RXCJ0524.4+0819 and other high extinction clusters have largely been avoided in WL studies due to concerns that their decreased visibility would make accurately measuring their WL signal too difficult. Indeed, there were many additional challenges that arose from working with a limited data sample, but with persistent debugging we were ultimately able to attain high-significance results for RXCJ0524.4+0819. Thus, this research can be contextualized as a proof of concept for larger studies; we demonstrated that analyzing the WL signal of high extinction galaxy clusters is feasible with enough observational data, and learned what types of obstacles and errors to expect when performing these analyses. This increases the number of sample clusters that can be analyzed via this method in the near-future, as high extinction clusters do not need to be ignored or discarded by default.

This was achieved by processing many deep DECam (Section 3.1) images of RXCJ0524.4+0819 using an adapted version of the *LSST Science Pipelines* image processing workflow (Section 4). We calibrated individual exposures with reference data (Section 4.2), created coadded images with improved depth (Section 4.3), and used measurements of these images (Section 4.4) to analyze the cluster's weak lensing signal (Section 4.5). We constructed overlays of the cluster's surface mass density on the optical image, profiles of the lensing intensity as a function of radius from the cluster's center, and histograms of the NFW best-fit mass prediction for RXCJ0524.4+0819.

6.1 Future Work

There are many ways in which future studies can build upon this work. First, there is room for subsequent analyses of RXCJ0524.4+0819 itself. Primarily, in order to get a more accurate mass estimate, the photometric redshifts of the background galaxies along the line of sight would be needed. Photometric redshifts are known for some galaxy clusters, but not generally for high extinction ones. Determining redshifts is more difficult for high extinction clusters because it requires having observational data in all filter bands. This is a challenge because some of the filters have intrinsically higher extinction magnitudes, such as the u- and g-bands. As a result, if a high extinction cluster is observed it is not commonly done in all bands. For example, of the 20+ high extinction clusters we looked at, not one had deep images in all filters (many of them had some exposures in most of the common DECam filters, but generally only a couple hundred seconds for each). In this sense, it will generally be easier to study the morphology of high extinction clusters and map their DM distributions, than to get highly accurate mass measurements. That being said, taking DECam data of high extinction clusters in all filters is certainly doable and would allow us

to calculate photometric redshifts of the background sources to calculate the actual mass.[30] Also, having exposures in more filters would simply improve the depth of our coadded images and lead to better results overall.

It would also benefit the study of RXCJ0524.4+0819 to have a deep X-ray image that could be overlaid on the optical–surface density map image shown in Figure 14. This is commonly done as a supplementary point of visual comparison between the WL and X-ray signals, and perhaps it would provide more insight into the nature of the offset between RXCJ0524.4+0819's WL peak and BCG. We would be curious to see how the X-ray distribution lines up relative to the two, as "the relative distributions of cluster dark matter, X-rays, and BCGs can place strong limits on potential dark matter models" [1, p. 15]. Unfortunately, as mentioned in Sections 3.2 and 4.5, there is currently no CHANDRA image available for this cluster, so either CHANDRA or another active X-ray telescope would have to observe it.

Second, in addition to RXCJ0524.4+0819, there are other high extinction clusters in our group's sample that have not been analyzed. Most notably, the cluster RXCJ1407.8-5100 has already been processed in the same manner described in Section 4, but yielded peculiar results. More details about RXCJ1407.8-5100 itself, as well as a discussion of its errored results and possible solutions, can be found in Appendix A. This cluster is the first high extinction one we recommend completing the analysis for, but there are other high extinction clusters in our database that could potentially have sufficient DECam data to be studied. The most promising remaining clusters are summarized in Appendix B.

Generally speaking, the most important future step is to analyze more clusters. Our underlying goal of using WL to probe galaxy clusters is to "constrain the relationship between WL mass and directly observable quantities in the local universe" [1, p. 15]. This requires a statistically significant collection of clusters for which we have multiple types of mass measurements. For example, the more observations and subsequent analyses that are performed in the optical/near-infrared and X-ray regime, the closer we are to quantifying the bias of X-ray estimates and getting a scaling relation between X-ray mass and actual mass. For high extinction clusters in particular, it seems like this will demand even more observational data, as a relatively lower fraction of their exposures end up usable. These large galaxy cluster studies provide insight into areas beyond just the cluster masses themselves. They allow us to better understand galaxy cluster formation [5], substructure, and evolution [16], as well as constrain different models of DM and cosmology [3, 9, 12, 18].

One of the largest upcoming observational efforts is the Vera C. Rubin Observatory Legacy Survey of Space and Time (LSST) for which the image processing pipeline we used was originally designed. LSST will carry out a diverse set of surveys, but the one focused on galaxy clusters is intentionally avoiding those near the galactic plane because of extinction. However, there is one survey that is looking at stars in the galactic plane, so one could potentially use images from that

[30] For a deep neural network approach to measuring photometric redshifts, see [33].

survey to study the high extinction galaxy clusters behind the stars. A survey dedicated to imaging high extinction clusters would allow the process outlined in this paper to be repeated on a much larger scale, looking at the results of many clusters to see what trends emerge. Perhaps one would find an upper bound extinction value that is the limit for a cluster to be analyzed with current technology. Also, if there were revealed to be some noticeable bias in high extinction clusters only, one would be able to quantify and correct for it. Whether or not these clusters should be a top priority when there lower extinction clusters (easier and cheaper in terms of telescope time) still to be studied, is a valid debate. Either way, we have shown that high extinction clusters need not be preemptively rejected if imaging data is available—they can be valuable weak lensing laboratories for dark matter research.

We are looking forward to what is next for high extinction galaxy clusters.

References

[1]Jacqueline McCleary, Ian dell'Antonio, and Anja von der Linden, "Dark matter distribution of four low-z clusters of galaxies", The Astrophysical Journal **893**, Publisher: American Astronomical Society, 8 (2020).

[2]Peter Schneider, *Extragalactic astronomy and cosmology: an introduction*, Second (Springer-Verlag, Berlin Heidelberg, 2006).

[3]Steven W. Allen, August E. Evrard, and Adam B. Mantz, "Cosmological parameters from observations of galaxy clusters", Annual Review of Astronomy and Astrophysics **49**, 409–470 (2011).

[4]Peter Schneider, "Weak gravitational lensing", arXiv:astro-ph/0509252 **33**, version: 1, 269–451 (2006).

[5]Andrey Kravtsov and Stefano Borgani, "Formation of galaxy clusters", Annual Review of Astronomy and Astrophysics **50**, 353–409 (2012).

[6]D. Wittman, "Weak lensing", arXiv:astro-ph/0208063 (2002).

[7]Binyang Liu, "Weak and not so weak lensing: shear calibration and dark matter structure in galaxy clusters", PhD thesis (Brown University, Providence, Rhode Island, May 2020), 104 pp.

[8]D. Wittman et al., "First results on shear-selected clusters from the deep lens survey: optical imaging, spectroscopy, and x-ray followup", The Astrophysical Journal **643**, 128–143 (2006).

[9]David Harvey et al., "Observable tests of self-interacting dark matter in galaxy clusters: BCG wobbles in a constant density core", Monthly Notices of the Royal Astronomical Society **488**, 1572–1579 (2019).

[10]M. James Jee et al., "MC2: CONSTRAINING THE DARK MATTER DISTRIBUTION OF THE VIOLENT MERGING GALAXY CLUSTER CIZA j2242.8+5301 BY PIERCING THROUGH THE MILKY WAY", The Astrophysical Journal **802**, Publisher: American Astronomical Society, 46 (2015).

[11]Linda Ostman, Ariel Goobar, and Edvard Mortsell, "Extinction properties of lensing galaxies", Astronomy & Astrophysics **485**, 403–415 (2008).

[12]Hakon Dahle, "The cluster mass function from weak gravitational lensing", The Astrophysical Journal **653**, Publisher: American Astronomical Society, 954–962 (2006).

[13]R. Sadat, "Clusters of galaxies and mass estimates", **126**, Conference Name: From Quantum Fluctuations to Cosmological Structures Place: eprint: arXiv:astro-ph/9702050, 349 (1997).

[14]August E. Evrard, Christopher A. Metzler, and Julio F. Navarro, "Mass estimates of x-ray clusters", The Astrophysical Journal **469**, 494 (1996).

[15]Browse Software Development Team, *MCXC - MCXC meta-catalog of x-ray detected clusters of galaxies*, HEASARC, (Jan. 29, 2020) https://heasarc.gsfc.nasa.gov/W3Browse/rosat/mcxc.html.

[16]J. McCleary, I. dell'Antonio, and P. Huwe, "MASS SUBSTRUCTURE IN ABELL 3128", The Astrophysical Journal **805**, Publisher: American Astronomical Society, 40 (2015).

[17]Eric J. Hallman et al., "Challenges for precision cosmology with x-ray and sunyaev-zeldovich effect gas mass measurements of galaxy clusters", The Astrophysical Journal **648**, Publisher: IOP Publishing, 852 (2006).

[18]Nevin N. Weinberg and Marc Kamionkowski, "Constraining dark energy from the abundance of weak gravitational lenses", Monthly Notices of the Royal Astronomical Society **341**, 251–262 (2003).

[19]Matthias Bartelmann and Peter Schneider, "Weak gravitational lensing", Physics Reports **340**, 291–472 (2001).

[20]Julio F. Navarro, Carlos S. Frenk, and Simon D. M. White, "A universal density profile from hierarchical clustering", The Astrophysical Journal **490**, Publisher: American Astronomical Society, 493–508 (1997).

[21]Anna Monna, "Investigating galaxies in and behind Galaxy Clusters using Strong Gravitational Lensing", PhD thesis (Ludwig-Maximilians-Universität München, Feb. 24, 2015).

[22]Ian Dell'Antonio and Shenming Fu, *Run steps - a brief guide.pdf*, July 20, 2020.

[23]*Dark energy camera (DECam) — CTIO*, http://www.ctio.noao.edu/noao/content/Dark-Energy-Camera-DECam.

[24]B. Flaugher et al., "THE DARK ENERGY CAMERA", The Astronomical Journal **150**, Publisher: American Astronomical Society, 150 (2015).

[25]LSST contributors, *Getting started with the LSST science pipelines — LSST science pipelines*, LSST Science Pipelines, in collab. with Shenming Fu, (Dec. 10, 2020) https://pipelines.lsst.io/getting-started/index.html#getting-started-tutorial.

[26]Brown University Center for Computation and Visualization, *High-performance computing (oscar)*, Brown Center for Computation and Visualization, https://ccv.brown.edu.

[27]Astropy Collaboration et al., "The astropy project: building an open-science project and status of the v2.0 core package", The Astronomical Journal **156**, _eprint: 1801.02634, 123 (2018).

[28]Astropy Collaboration et al., "Astropy: a community python package for astronomy", Astronomy & Astrophysics **558**, _eprint: 1307.6212, A33 (2013).

[29]A. Ginsburg et al., "Astroquery: an astronomical web-querying package in python", The Astronomical Journal **157**, _eprint: 1901.04520, 98 (2019).

[30]Michael Waskom and the seaborn development team, *Seaborn: statistical data visualization*, version JOSS paper (latest), Mar. 29, 2021.

[31]CFHT Elixer Project, *Fringe and low-order additive corrections in wide-field mosaic cameras*, The Elixer Project, https://www.cfht.hawaii.edu/Instruments/Elixir/fringes.html.

[32]Christopher Hirata and Uroš Seljak, "Shear calibration biases in weak-lensing surveys", Monthly Notices of the Royal Astronomical Society **343**, 459–480 (2003).

[33]B. Hoyle, "Measuring photometric redshifts using galaxy images and deep neural networks", Astronomy and Computing **16**, 34–40 (2016).

Appendices

A Related Study: RXCJ1407.8-5100

Another high extinction galaxy cluster in our group's sample is RXCJ1407.8-5100. Although it is significantly farther from the galactic plane, it has slightly larger extinction magnitudes than RXCJ0524.4+0819's listed in Table 2. It also has a fairly high star-density, with 77 stars brighter than $mag < 13$, over twice as many as RXCJ0524.4+0819's number of 33. Moreover, unlike RXCJ0524.4+0819, RXCJ1407.8-5100 is one of the brightest clusters in our sample in terms of X-ray luminosity, corresponding to a mass value twice that of RXCJ0524.4+0819. The values for RXCJ1407.8-5100's properties are given in Table 3 below.

RA	**Dec**	**Redshift (z)**	**L_{X500} (erg/s)**	**M_{X500} ($M_\odot$)**
$14^h7^m52.5^s$	$-51°00'33''$	0.0966	3.9186650×10^{44}	4.40060×10^{14}

Table 3. Properties of RXCJ1407.8-5100: right ascension, declination, redshift, X-ray luminosity, and X-ray mass. Values from: [15].

RXCJ1407.8-5100 has been processed through the same image processing pipeline as described in Section 4, but its results are more questionable. Figure 17 shows the final optical-surface mass density overlay for this cluster (middle range: (4,4)–(7,7)). As one can clearly see, there is an issue in the centermost region, where a significant distortion has emerged, in green. This is not an authentic reflection of the cluster's structure in the optical and it instead most likely a result of errors in the images that were inputted into coaddition. Tracing the distortion back through the pipeline, it was found that this shape was only present in the r-band (see Figure 18).

Looking through each of the r filter's PSF-matched temporary exposures (*tempExp*) for the center patches, a number of abnormal exposures were indeed found. These images had one quarter to half of the image distorted, appearing as a completely blown-out section with a strong gradient from white to dark grey. As an additional check, we examined the temporary exposures in the other available filters: g, i, and z. The g-band images had no significant issues and the i- and z-bands only had a couple blank images. The specific problematic visits in the r, i, and z filters were removed from their corresponding *.list* catalogs of successful visits that gets passed onto the coadd assembly step.

The next step would be to complete the coaddition stage (Section 4.3) again, rerunning the *assembleCoadd* process. If the aforementioned corrections are successful, this cluster could quickly be added to the short list of high extinction clusters for which the lensing signal, density map overlay, and mass estimate have been successfully measured. (For completeness, we include the fitted shear profile and mass fit histogram for RXCJ1407.8-5100 for the middle range ((4,4)–(7,7)) below. As expected, these results yield very poor fits because of the image's significant problem.)

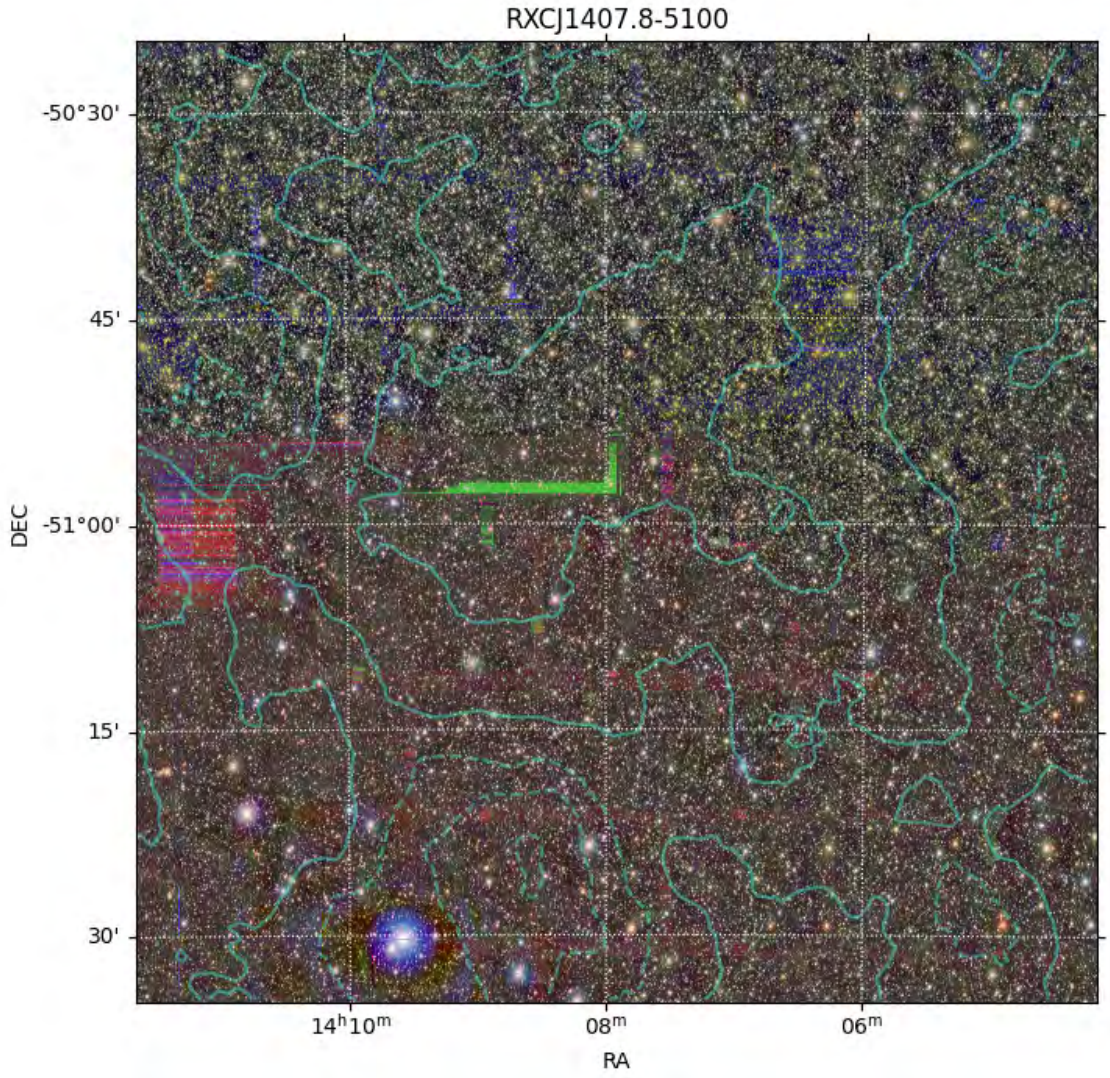

Figure 17. Overlay of RXCJ0524.4+0819's surface mass overdensity contours (in light blue) on the optical image. Note the increased star-density throughout the FOV. There is a significant error in the center patches (green "sideways L" distortion).

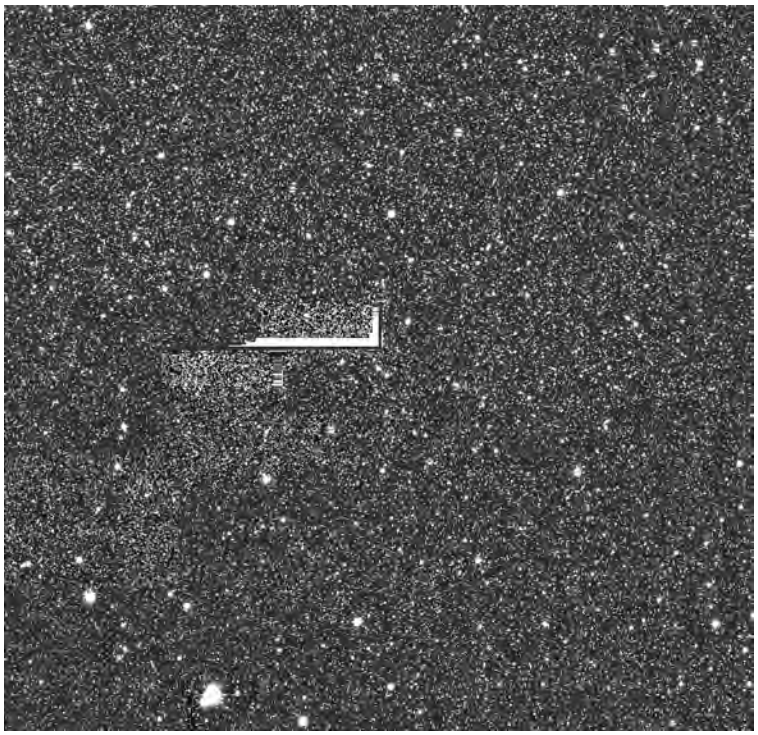

Figure 18. Stacked coadded image for the r filter, middle range: (4,4)–(7,7). The error visible in Figure 17 can be seen here.

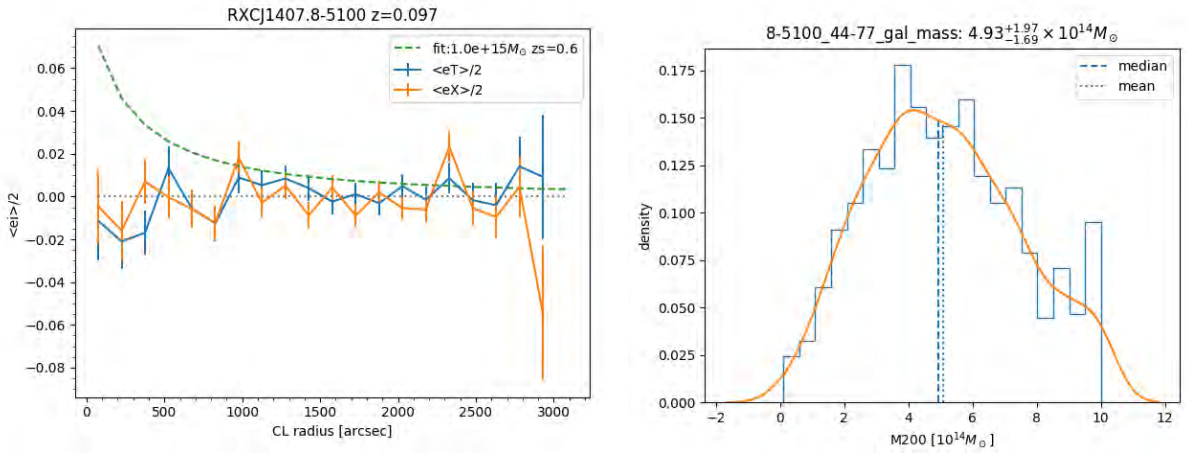

(a) Shear profile of RXCJ0524.4+0819 with an NFW fit. The signal is an extremely poor fit, likely a reflection of the distorted central patches which are crucial in mapping the WL signature. (See Figure 15 for graph details such as line color and axes.)

(b) Mass fit histogram of RXCJ0524.4+0819. Although the average value is technically consistent with the cluster's X-ray mass, the curve has very large error spread of almost $2 \times 10^{14} M_\odot$. These results are thus not significant. (See Figure 16 for graph details such as line color and axes.)

Figure 19. Mass estimates of RXCJ1407.8-5100 from the shear profile and global mass fit processes (see Section 4.5) for the middle range: (4,4)–(7,7).

B Additional High Extinction Candidates

In addition to both the cluster this study focused on, RXCJ0524.4+0819, and the cluster RXCJ1407.8-5100 discussed above in Appendix A, there are more clusters in our database that are yet to be measured and analyzed. These clusters and their relevant observational details are listed in Table 4, by descending X-ray luminosity.

Extinction (magnitudes), **Exposure Time (s)**							
Filter / **Cluster**	u	g	r	i	z	Y	VR
RXCJ0338.6+0958	1.741, -	1.357, -	0.939, **2000**	0.697, -	0.519, -	0.435,	-, **2800**
RXCJ1839.8-2108	1.888, -	1.471, -	1.018, -	0.756, -	0.563, -	0.471, -	-, **1200**
RXCJ0448.0+1037	2.010, -	1.567, -	1.084, -	0.805, -	0.599, -	0.502, -	-, **2900**
RXCJ1518.3-4632	1.483, -	1.155, **1150**	0.799, **1800**	0.594, -	0.442, -	0.370, -	-, -
RXCJ1535.1-4658	1.894, -	1.476, **1700**	1.021, **2000**	0.759, -	0.564, -	0.473, -	-, **800**

Table 4. Extinctions and observation times in each DECam filter for multiple high extinction clusters. Ordered by X-ray luminosity (descending).

Based on the DECam data available for these remaining clusters, I would recommend studying them in the following order (with room for reconsideration): RXCJ1535.1-4658, RXCJ1518.3-4632, RXCJ0338.6+0958 (needed larger radius of 2 instead of 1.5), and possibly RXCJ0448.0+1037. Beyond these candidates, there are many more high extinction clusters in our sample that have either a couple hundred seconds of exposure in each filter, a couple hundred seconds total, or no DECam data at all. Most likely, all of these clusters do not have enough data across multiple filters to achieve accurate lensing results, if any result at all.

C Omitted Figures

For the final overlay results in Section 5.1 (and the optical image example in subsection 4.3.1, figure 12), we use the composite optical image generated with i/VR/i because that is the deepest set of at least two distinct filters. However, additional optical images were created using different combinations of two or three filters. These color combinations offer alternative perspectives on the contrast within the field, and shift the sensitivity towards sources of different frequencies.

C.1 Color Optical Images

The second deepest filter combination was i, VR, and VR. The optical image in this color scheme for the central region ((5,5)–(6,6)) is shown in Figure 20.

For RXCJ0524.4+0819, we did have three different filters. As discussed in Sections 4.3 and 4.3.1, we avoided using the r-band for the composite images. Although the image is less consistent overall and has discolored regions, composing a color image using the i, VR, and r filters produces a more colorful depiction of the cluster (see Figure 21).

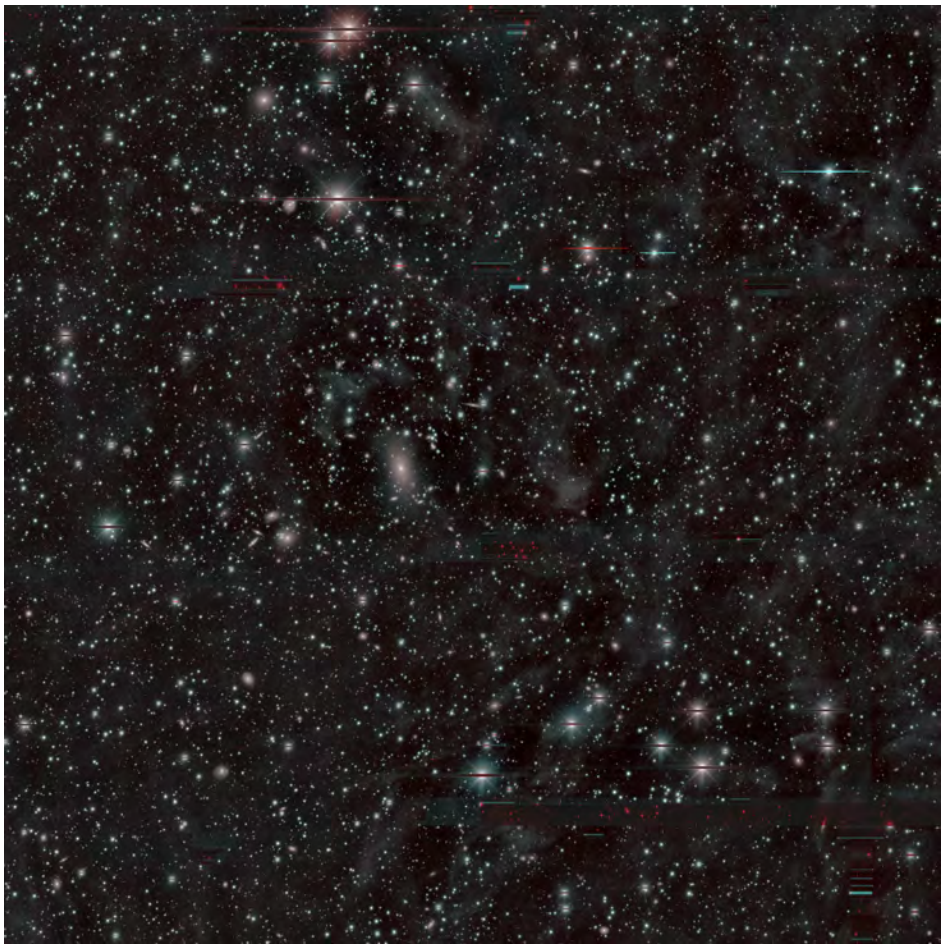

Figure 20. Color optical image for the central region ((5,5)–(6,6)) using the i/VR/VR filters.

C.2 Optical–Surface Density Map Overlays

In section 5.1, only the middle range overlay image was presented as it was the widest range that had no significant distortions on the edges from limited data. That being said, it is still beneficial to visualize the central and outer ranges to examine the WL peak–BCG offset and cluster environment in more detail. These overlays are presented in Figures 22 and 23, respectively.

Lastly, other orderings of the deepest two filters, i and VR, produce results with different color emphases. A particularly distinct color combination is VR/i/VR; the central overlay for this filter set is shown in Figure 24.

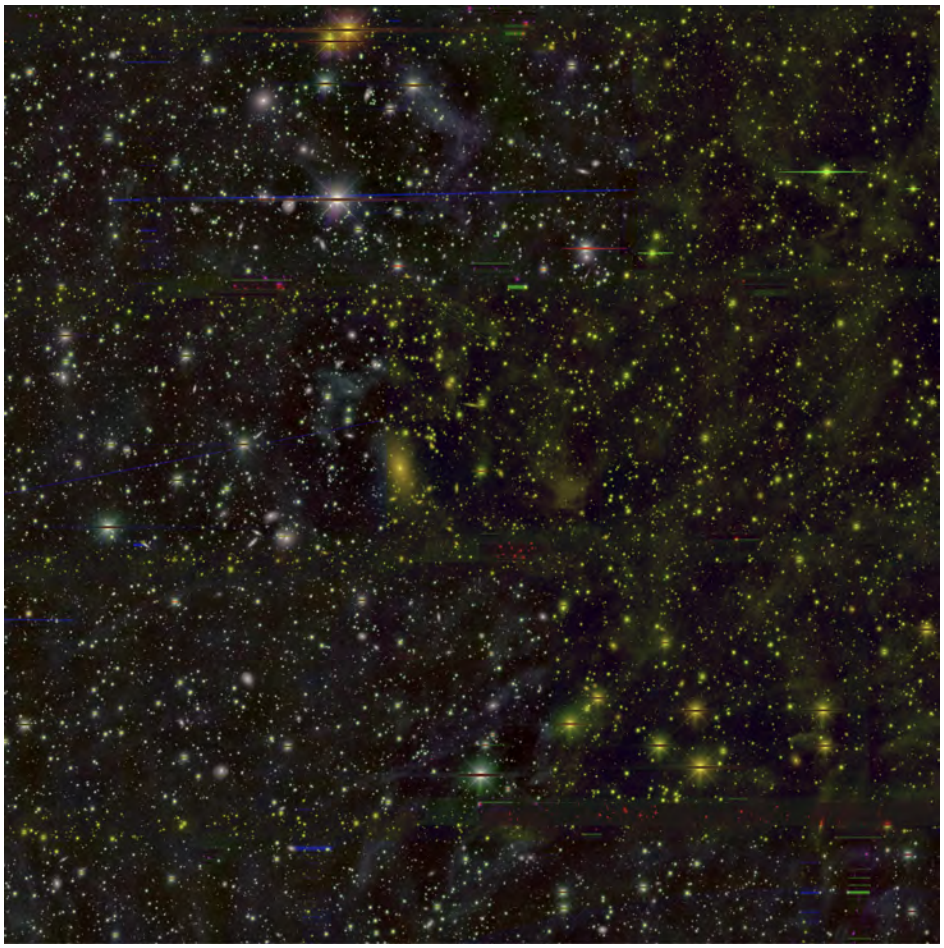

Figure 21. Color optical image for the central region ((5,5)–(6,6)) using the i/VR/r filters. The yellow discoloration in the right half of the image is due to the r filter image missing sections.

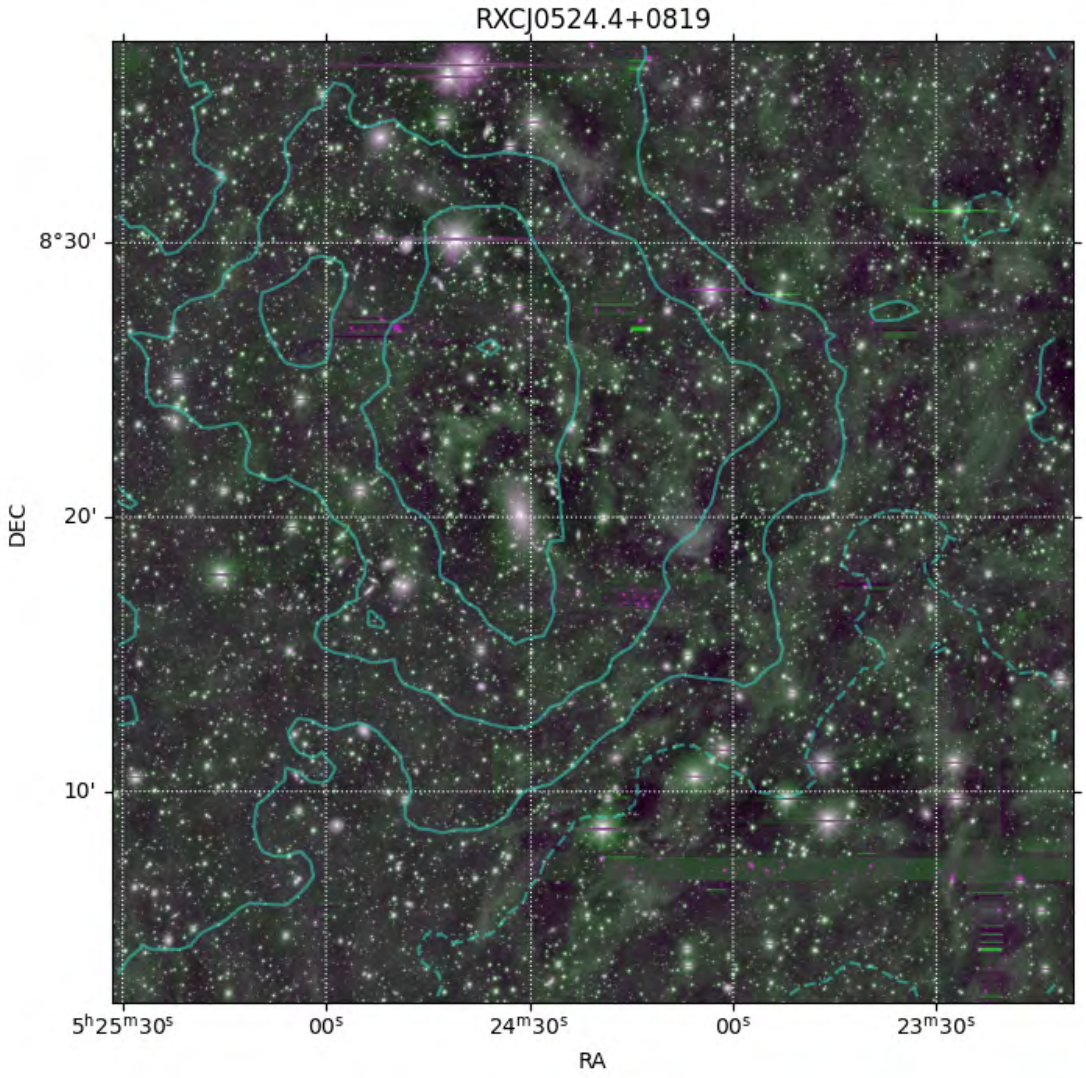

Figure 22. Overlay of the surface mass overdensity map contours (in light blue) on the optical image created using the i/VR/i filters for the central range: (5,5)–(6,6). Note the offset between the WL peak and BCG.

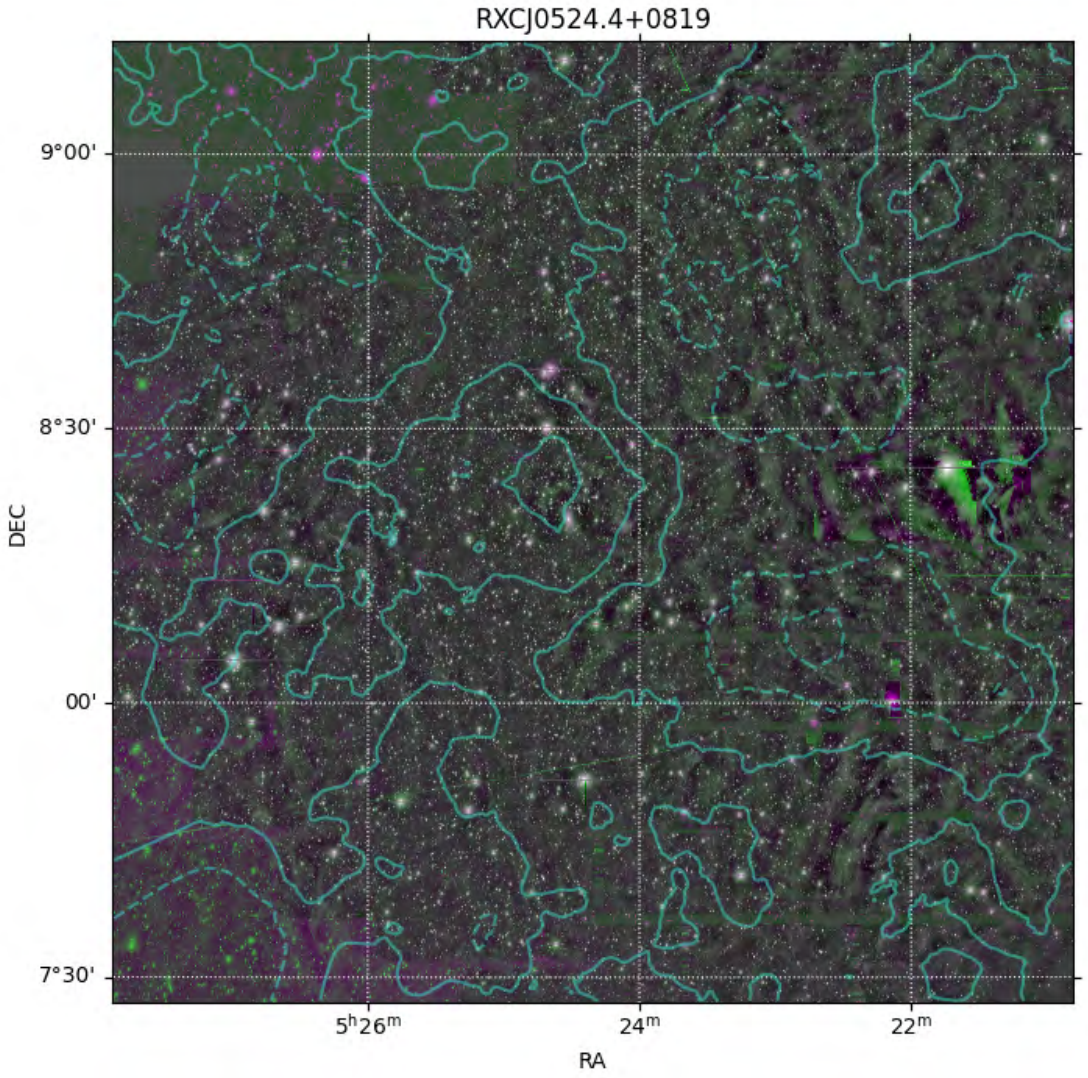

Figure 23. Overlay of the surface mass overdensity map contours (in light blue) on the optical image created using the i/VR/i filters for the outer range: (3,3)–(8,8). There are distortions/artifacts in the upper left corner and right middle of the image from incomplete data in those regions.

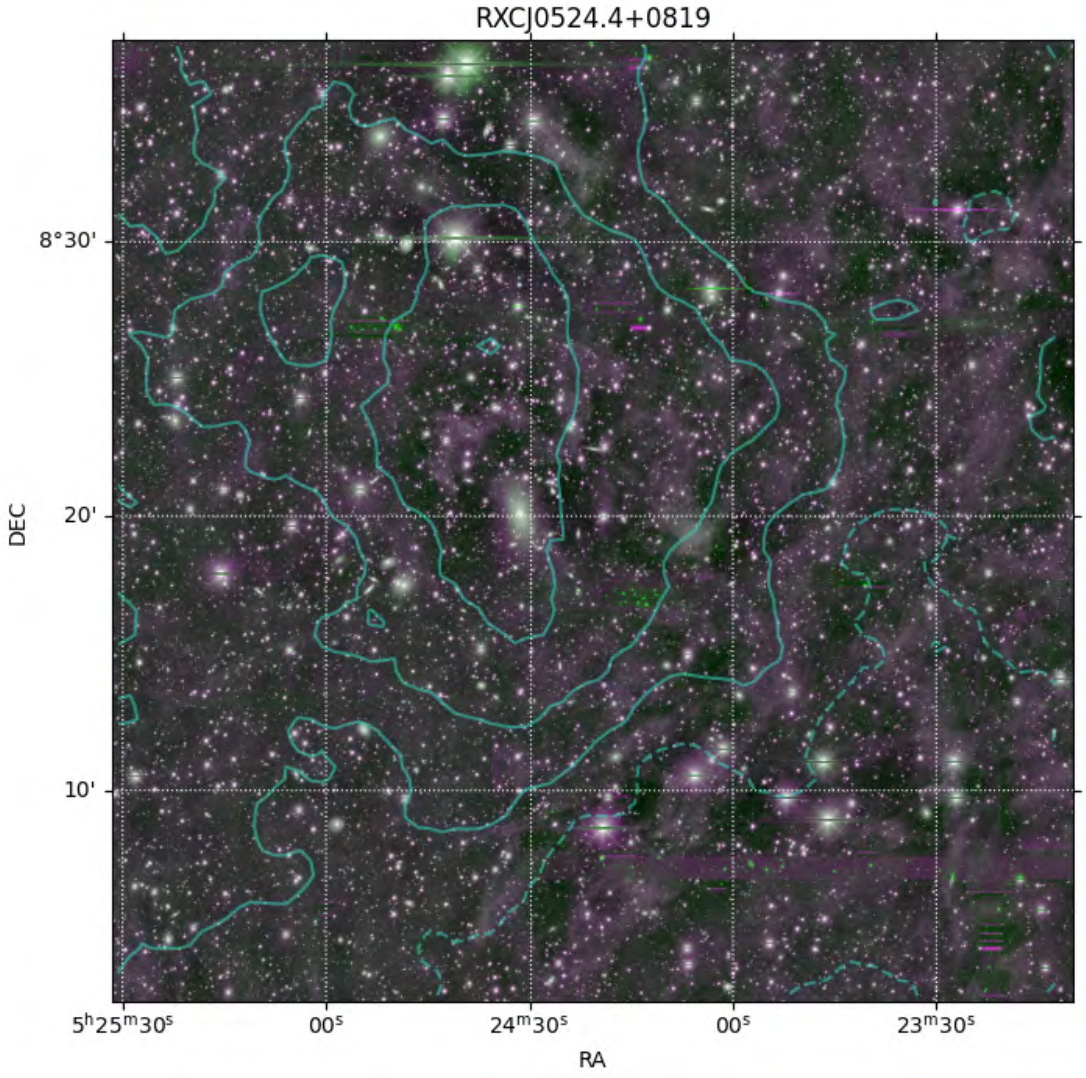

Figure 24. Overlay of the surface mass overdensity map contours (in light blue) on the optical image created using the VR/i/VR filters, inner range: (5,5)–(6,6).